

# Applications of magnetic-field modeling for hybrid MEG and MRI

---

Antti Mäkinen



# Applications of magnetic-field modeling for hybrid MEG and MRI

**Antti Mäkinen**

A doctoral dissertation completed for the degree of Doctor of Science (Technology) to be defended, with the permission of the Aalto University School of Science, at an examination held at the lecture hall F239a of the school on the 18th of November 2020 at 3 pm. The examination is publicly available via a remote connection, <https://aalto.zoom.us/j/62702105698>

**Aalto University**  
**School of Science**  
**Department of Neuroscience and Biomedical Engineering**

**Supervising professor**

Professor Risto Ilmoniemä, Aalto University, Finland

**Thesis advisor**

Professor Risto Ilmoniemä, Aalto University, Finland

**Preliminary examiners**

Professor Samu Taulu, University of Washington, USA

Professor Samuli Siltanen, University of Helsinki, Finland

**Opponent**

Professor Matthew Rosen, Athinoula A. Martinos Center for Biomedical Imaging, USA

Aalto University publication series

**DOCTORAL DISSERTATIONS** 174/2020

© 2020 Antti Mäkinen

ISBN 978-952-64-0109-6 (printed)

ISBN 978-952-64-0110-2 (pdf)

ISSN 1799-4934 (printed)

ISSN 1799-4942 (pdf)

<http://urn.fi/URN:ISBN:978-952-64-0110-2>

Unigrafia Oy

Helsinki 2020

Finland



**Author**

Antti Mäkinen

**Name of the doctoral dissertation**

Applications of magnetic-field modeling for hybrid MEG and MRI

**Publisher** School of Science

**Unit** Department of Neuroscience and Biomedical Engineering

**Series** Aalto University publication series DOCTORAL DISSERTATIONS 174/2020

**Field of research** Biomedical Engineering, Physics

**Manuscript submitted** 20 August 2020

**Date of the defence** 18 November 2020

**Permission for public defence granted (date)** 15 October 2020

**Language** English

☐ **Monograph**

☒ **Article dissertation**

☐ **Essay dissertation**

**Abstract**

This Thesis concentrates on methods for modeling and analyzing the magnetic field in magnetic brain imaging. The work is motivated by the combination of two brain imaging modalities, magnetoencephalography (MEG) and magnetic resonance imaging (MRI), in a single MEG–MRI device. In magnetoencephalography, brain functions are studied by recording the magnetic-field distribution generated by electrical brain activity. With magnetic resonance imaging, the structure of the head can be analyzed. The combination of these two imaging methods is enabled by applying ultra-low magnetic fields for MRI (ULF MRI). Besides the imaging structure, ultra-low-field MRI can be made sensitive to the magnetic field generated by small currents, enabling current density imaging (CDI). This method can be utilized to estimate the current flow in the head, which is needed for modeling the neuronal magnetic field in MEG and especially the electric field studied by electroencephalography (EEG).

Magnetic-field modeling was first applied for spatial calibration of ULF MRI, which enables enhancing the spatial accuracy of MEG when measured with the hybrid MEG–MRI device. Second, MR imaging of magnetic fields generated by injected currents inside the human head was simulated to study the performance of CDI. Third, the electric and magnetic fields generated by brain activity were analyzed to study the effect of field sampling in MEG and EEG. Last, general computational tools were developed for modeling and designing magnetic fields produced, e.g., by the electromagnetic coils used in MRI. Altogether, this Thesis provides computational and methodological tools that facilitate the analysis and design of biomagnetic experiments for brain research.

**Keywords** magnetic resonance imaging, magnetoencephalography, magnetic field, computational methods

**ISBN (printed)** 978-952-64-0109-6

**ISBN (pdf)** 978-952-64-0110-2

**ISSN (printed)** 1799-4934

**ISSN (pdf)** 1799-4942

**Location of publisher** Helsinki

**Location of printing** Helsinki **Year** 2020

**Pages** 130

**urn** <http://urn.fi/URN:ISBN:978-952-64-0110-2>



**Tekijä**

Antti Mäkinen

**Väitöskirjan nimi**

Magneetikentän mallinnuksen sovelluksia yhdistettyä MEG–MRI-kuvantamista varten

**Julkaisija** Perustieteiden korkeakoulu

**Yksikkö** Neurotieteen ja lääketieteellisen tekniikan laitos

**Sarja** Aalto University publication series DOCTORAL DISSERTATIONS 174/2020

**Tutkimusala** Lääketieteellinen tekniikka, fysiikka

**Käsikirjoituksen pvm** 20.08.2020

**Väitöspäivä** 18.11.2020

**Väittelyluvan myöntämispäivä** 15.10.2020

**Kieli** Englanti

☐ **Monografia**

☒ **Artikkeliväitöskirja**

☐ **Esseeväitöskirja**

**Tiivistelmä**

Tämä väitöskirja käsittelee menetelmiä magneettikentän mallinnukseen ja analysointiin magneettista aivokuvantamista varten. Motivaationa tehdyille tutkimukselle toimii MEG–MRI hybridikuvantamislaitte, joka yhdistää magnetoenkefalografian (MEG) ja magneettikuvauksen (MRI). Magnetoenkefalografiassa tutkitaan aivojen toimintaa niiden sähköisen aktiivisuuden synnyttämän magneettikentän avulla. Magneettikuvaus puolestaan antaa tietoa aivojen rakenteesta. Nämä menetelmät voidaan yhdistää madaltamalla magneettikuvauksessa käytettäviä magneettikenttiä ultramatalalle tasolle (ultra-matalan kentän magneettikuvaus, ULF MRI). Ultra-matalan kentän magneettikuvauksella voidaan myös kuvata aivoissa kulkevia sähkövirtoja, koska kyseinen kuvausmenetelmä voidaan tehdä herkäksi näiden virtojen synnyttämälle magneettikentälle. Virrankuvantamista (CDI) voidaan hyödyntää esimerkiksi pään johtavuusrakenteen kartoittamiseen, mitä tarvitaan aivojen synnyttämän magneettikentän ja erityisesti sähkökentän mallintamiseen.

Magneettikentän mallinnusta hyödynnettiin ensiksi ultra-matalan kentän magneettikuvien avaruudelliseen kalibrointiin MEG–MRI-laitetta varten. Kalibrointimenetelmä takaa MEG:n paikkatarkkuuden parantamisen MEG–MRI-laitetta käytettäessä. Toisessa osatyössä päähän syötettävän virran synnyttämää magneettikenttää simuloitiin CDI-mittausten luotettavuuden analysointia varten. Kolmannessa osatyössä aivojen synnyttämää magneetti- ja sähkökenttiä analysoitiin kenttien näytteistyksen tutkimukseen. Viimeiseksi kehitettiin yleisiä laskennallisia työkaluja, joiden avulla magneettikenttiä voidaan mallintaa ja suunnitella haluttuja kenttämutoja synnyttäviä keloja esimerkiksi magneettikuvausta varten. Kokonaisuudessaan tämä väitöskirja tarjoaa laskennallisia ja metodologisia työkaluja, jotka helpottavat biomagneettisten aivotutkimusten suunnittelua ja analysointia.

**Avainsanat** magneettikuvaus, magnetoenkefalografia, magneettikenttä, laskennalliset menetelmät

**ISBN (painettu)** 978-952-64-0109-6

**ISBN (pdf)** 978-952-64-0110-2

**ISSN (painettu)** 1799-4934

**ISSN (pdf)** 1799-4942

**Julkaisupaikka** Helsinki

**Painopaikka** Helsinki

**Vuosi** 2020

**Sivumäärä** 130

**urn** <http://urn.fi/URN:ISBN:978-952-64-0110-2>



# Preface

This thesis work was mainly conducted at the Department of Neuroscience and Biomedical Engineering (NBE) of Aalto University. The work started in 2016 in an EU project called BREAKBEN, which was aimed to produce a new-generation MEG–MRI device. During this time, I managed to connect with multiple co-workers who helped me in getting this thesis work done.

I wish to thank my prof. Risto Ilmoniemi for the supervision of this Thesis. I had multiple insightful discussions with you. Most prominently, I remember you emphasizing the importance of understanding the basics, which I fully agree. I also want to thank Koos Zevenhoven for guidance, especially in my early days in the MEG–MRI group. I am grateful for all the people who have worked in the MEG–MRI project and, in particular, I wish to thank Iiro Lehto and Marko Havu for the shared experiences. My special thanks go to Gavriela Vranou. I learned a lot while advising your Master’s thesis.

I thank all the colleagues with whom I discussed and worked during the BREAKBEN project. Rainer Körber at PTB Berlin, who collaborated with our research group at Aalto during the project, gave me a chance to make a research visit at PTB. I really enjoyed your hospitality and the inspiring atmosphere in your group. I also wish to thank Nora Höfner and Jan Storm for the memorable visit and, of course, Peter Hömmen for the collaboration, which culminated in a research paper.

I would also like to thank Matti Stenroos for giving the opportunity to teach in many courses starting already in 2015 from the course of electromagnetic field theory. During these years, I had many useful discussions with you, Matti and also with the fellow teaching assistant Joonas Iivanainen. I thank you Joonas for the daily coffee breaks, which eventually turned into a research collaboration. Furthermore, I want to thank Prof. Lauri Parkkonen with whom I collaborated in the BREAKBEN project. The experience I gathered in that project inspired me to develop the `bfieldtools` package together with Rasmus Zetter and Joonas. Thank you Rasmus for the pleasant collaboration.

For financial support, I thank the Väisälä Foundation whose grant for

doctoral studies gave me the opportunity to finalize the different projects for this Thesis. I am grateful for the pre-examiners Samu Taulu and Samuli Siltanen for their thoughtful comments.

I want to thank my friends for organizing activities other than research whether it was a cruise with a karaoke competition, orienteering in the wild or playing badminton. Lastly, I thank my parents and my sister for encouraging me in my studies and, of course, my wife Viivi for the daily support and love.

Helsinki, October 2020,

Antti Mäkinen

# Contents

<b>Preface</b>	<b>1</b>
<b>Contents</b>	<b>3</b>
<b>List of Publications</b>	<b>5</b>
<b>Author's Contribution</b>	<b>7</b>
<b>Abbreviations</b>	<b>9</b>
<b>1. Introduction</b>	<b>11</b>
1.1 Aims of this Thesis . . . . .	12
<b>2. Background: Physics</b>	<b>13</b>
2.1 Quasistatic approximation of the electromagnetic field . .	13
2.2 Bioelectric and biomagnetic fields . . . . .	15
2.2.1 Source currents in a volume conductor . . . . .	15
2.2.2 Conductivity models and the forward problem .	16
2.3 Magnetization and magnetic resonance . . . . .	18
2.3.1 Fields and analogy to volume-conductor problems	18
2.3.2 Intrinsic magnetization in materials . . . . .	19
2.3.3 Magnetic resonance . . . . .	19
2.4 Magnetic field in free space . . . . .	21
2.4.1 Magnetic scalar potential . . . . .	21
2.4.2 Equivalent sources and their decomposition . .	21
2.4.3 Relation to multipole expansion . . . . .	22
2.5 Detection of magnetic field and magnetic sources . . . . .	23
2.5.1 Magnetic-field sensors . . . . .	23
2.5.2 Spatial sensitivity to magnetic sources . . . . .	24
<b>3. Background: Imaging</b>	<b>27</b>
3.1 Linear imaging systems . . . . .	27
3.2 MRI . . . . .	29

3.2.1	Encoding and reconstruction . . . . .	29
3.2.2	Multi-channel MRI . . . . .	30
3.3	MEG . . . . .	31
3.3.1	Minimum norm estimate . . . . .	31
3.3.2	Source estimation using additional prior information . . . . .	32
3.3.3	Spatial sampling . . . . .	34
3.4	Ultra-low-field MRI and MEG–MRI . . . . .	35
3.4.1	Basics principles of ultra-low-field MRI . . . . .	35
3.4.2	Current-density imaging . . . . .	36
3.4.3	Co-registration and Spatial Calibration of MEG and MRI . . . . .	37
<b>4.</b>	<b>Summary of Publications</b>	<b>39</b>
4.1	Publication I: "Automatic spatial calibration of ultra-low-field MRI for high-accuracy hybrid MEG–MRI" . . . . .	39
4.2	Publication II: "Evaluating the performance of ultra-low-field MRI for in-vivo 3D current density imaging of the human head" . . . . .	39
4.3	Publication III: "Spatial sampling of MEG and EEG revisited: From spatial-frequency spectra to model-informed sampling" . . . . .	40
4.4	Publication IV: "Magnetic-field modeling with surface currents. Part I. Physical and computational principles of bfieldtools" . . . . .	42
<b>5.</b>	<b>Discussion</b>	<b>45</b>
<b>6.</b>	<b>Conclusions</b>	<b>47</b>
	<b>References</b>	<b>49</b>
	<b>Publications</b>	<b>57</b>

# List of Publications

This Thesis consists of an overview and of the following publications which are referred to in the text by their Roman numerals.

- I** Antti J. Mäkinen\*, Koos C. J. Zevenhoven\*, and Risto J. Ilmoniemi. Automatic spatial calibration of ultra-low-field MRI for high-accuracy hybrid MEG–MRI. *IEEE Transactions on Medical Imaging*, Volume: 38, Issue: 6, June 2019.
- II** Peter Hömmen\*, Antti J. Mäkinen\*, Alexander Hunold, René Machts, Jens Haueisen, Koos C. J. Zevenhoven, Risto J. Ilmoniemi, and Rainer Körber. Evaluating the performance of ultra-low-field MRI for in-vivo 3D current density imaging of the human head. *Frontiers in Physics*, Volume 8, April 2020.
- III** Joonas Iivanainen\*, Antti J. Mäkinen\*, Rasmus Zetter, Matti Stenroos, Risto J. Ilmoniemi, and Lauri Parkkonen. Spatial sampling of MEG and EEG revisited: From spatial-frequency spectra to model-informed sampling. Submitted to *NeuroImage*, June 2020.
- IV** Antti J. Mäkinen, Rasmus Zetter, Joonas Iivanainen, Koos C. J. Zevenhoven, Lauri Parkkonen, and Risto J. Ilmoniemi. Magnetic-field modeling with surface currents. Part I. Physical and computational principles of bfieldtools. *Journal of Applied Physics*, Volume 128, August 2020.

\*These authors contributed equally to the study.



# Author's Contribution

## **Publication I: “Automatic spatial calibration of ultra-low-field MRI for high-accuracy hybrid MEG–MRI”**

The calibration method was aimed to meet the goals of the MEG–MRI project, which was conceived by RI, and in which this thesis work was conducted. KZ came up with the main idea for the method and provided some software for the numerical simulations. The Author implemented and carried out the simulations, developed the method further, and wrote the manuscript. KZ and RI provided comments for writing the manuscript.

## **Publication II: “Evaluating the performance of ultra-low-field MRI for in-vivo 3D current density imaging of the human head”**

The Author, PH, and RK conceived the study. AH, RM, and JH developed the head model and performed FEM simulations. The Author and PH performed the MRI simulations and analyzed the results. They wrote the manuscript together with input from all co-authors.

## **Publication III: “Spatial sampling of MEG and EEG revisited: From spatial-frequency spectra to model-informed sampling”**

The Author and JI designed the study and wrote the manuscript. The Author's main responsibility was to develop the theory. With the help of the Author, JI conducted most of the simulations and analyzed the data. MS provided tools for the field computations and contributed to structuring the manuscript. All authors provided feedback and revised the text.

## **Publication IV: “Magnetic-field modeling with surface currents. Part I. Physical and computational principles of bfieldtools”**

The Author formulated the computational framework together with RZ and JI. He carried out the analytical calculations and developed most of the basic-level program code implementing the formulas presented in the manuscript. The Author wrote the manuscript with input from all co-authors.



# Abbreviations

**3D** three-dimensional

**BEM** boundary-element method

**CDI** current-density imaging

**CSF** cerebrospinal fluid

**DFT** discrete Fourier transform

**EEG** electroencephalography

**FEM** finite-element method

**FFT** fast Fourier transform

**MEG** magnetoencephalography

**MNE** minimum-norm estimate

**MR** magnetic resonance

**MRI** magnetic resonance imaging

**NCI** neuronal current imaging

**OPM** optically-pumped magnetometer

**SNR** signal-to-noise ratio

**SRF** spatial-response function

**ULF** ultra-low-field

**SQUID** superconducting quantum-interference device



# 1. Introduction

Electricity is a fundamental component in the living human body. Electric signals in the nerve cells enable the communication of different body parts, all controlled by the brain. The electric activity in the brain can be studied non-invasively by electroencephalography (EEG) [1], i.e., by recording the electric potential differences on the scalp of the head. The electric current associated with the activity also generates a magnetic field which can be measured with magnetic-field sensors outside the head. The measurement of the magnetic field generated by the electrical brain activity is known as magnetoencephalography (MEG) [2].

In a limited sense, as these methods provide spatial information of the brain activity, they can be seen as brain imaging methods. They also provide real-time temporal information which is essential for studying how the brain works. Understanding the capabilities and limitations of these methods requires understanding the electromagnetic field.

In this work, I mainly concentrate on methods that measure the magnetic field generated in the brain. Besides MEG, another imaging method that involves the magnetic field is magnetic resonance imaging (MRI), which can be used to study the structure of the brain. In MRI, the field is generated by the nuclei of hydrogen atoms magnetized in a large external magnetic field. The strength of the resulting magnetization depends on the tissue type enabling differentiating between different tissues in MR images.

In MRI, it is possible to actively manipulate the magnetization, which provides a way for highly controllable spatial encoding and localization of the field source into small volume elements. On the contrary, in MEG measures only passively the magnetic field generated by the brain activity. To make inference of the brain activity itself, MEG requires a physical model for the electric current distributions responsible for the field. This model includes the structure of the head, which is usually derived from MR images.

Since modeling of MEG is intertwined with MRI and both methods measure the magnetic field, MEG would benefit if MRI could be performed

in the same device. To combine MEG and MRI [3, 4], the magnetic fields associated with MR imaging need to be lowered substantially, down to the magnitude of the Earth’s field. The resulting modality is known as ultra-low-field MRI (ULF MRI) [5, 6]. Besides the combination of the two imaging methods, ULF MRI offers unique possibilities for brain imaging such as the capability of direct imaging of current distributions inside the head.

## 1.1 Aims of this Thesis

This Thesis aims to facilitate the analysis and design of biomagnetic experiments and imaging by developing computational and methodological tools. The aims of the individual studies are listed below.

- I** To develop a method for accurate spatial calibration of ULF-MR images for hybrid MEG–MRI device. To verify and assess the method using numerical simulations.
- II** To understand and quantify the signal-to-noise ratios of the field reconstructions derived from zero-field-encoded CDI data. To determine whether existing ULF-MRI systems are adequate for current-density reconstructions.
- III** To analyze spatial sampling of EEG and MEG on general curved surfaces. To quantify the beneficial number of samples and the benefit of optimizing the sampling configuration.
- IV** To develop general computational tools for modeling magnetic fields using surface currents. To describe the computational principles of the developed software.

## 2. Background: Physics

In this Chapter, I describe the necessary physics for understanding the magnetic measurements in MEG and MRI. I start with the quasistatic approximation of the electromagnetic field applicable to both bioelectromagnetic measurements and ultra-low-field MRI. I describe how the quasistatic fields are generated in the two modalities and explain the magnetic resonance phenomenon from the classical perspective. Additionally, I discuss modeling the magnetic field in the free space. I finish this Chapter by analyzing the spatial sensitivity of magnetic-field sensors to magnetization and electric sources in the brain.

### 2.1 Quasistatic approximation of the electromagnetic field

Static magnetic and electric fields describe a special state of the electromagnetic field, where the rate of change of the field sources is negligible. In this state, the magnetic field  $\vec{B}(\vec{r})$  arises solely from electric currents, described by the current density  $\vec{J}(\vec{r})$  and the electric field  $\vec{E}(\vec{r})$  originates from the charge density  $\rho(\vec{r})$ . In the magnetoquasistatic approximation [7, 8], the electric field can additionally originate from a time-varying magnetic field but a time-varying electric field as a source of the magnetic field is considered negligible. Under this approximation, the physics of the fields are described by the following four Maxwell's equations

$$\text{Gauss' law} \quad \nabla \cdot \vec{E} = \frac{\rho}{\epsilon_0} \quad (2.1)$$

$$\text{Faraday's law} \quad \nabla \times \vec{E} = -\frac{\partial \vec{B}}{\partial t} \quad (2.2)$$

$$\text{Gauss law for } \vec{B} \quad \nabla \cdot \vec{B} = 0 \quad (2.3)$$

$$\text{Ampère's law} \quad \nabla \times \vec{B} = \mu_0 \vec{J} \quad (2.4)$$

where  $\epsilon_0$  is the electric permittivity and  $\mu_0$  the magnetic permeability in the free space. In addition to Maxwell's equations, the electric field and the current density are related by Ohm's law

$$\vec{J} = \sigma \vec{E}, \quad (2.5)$$

where  $\sigma$  is the conductivity of the material or tissue.

Neglecting the effect of displacement currents  $\epsilon \frac{\partial \vec{E}}{\partial t}$  in Ampère's law is justified by the relatively short time constant  $\epsilon/\sigma$  for the redistribution of charges in a linearly-polarized conductor [9, 7]. Here,  $\epsilon$  is the material permittivity including the electric polarization. For example, in the brain, with material parameters  $\sigma = 0.3 \text{ S/m}$  and  $\epsilon = 10^5 \epsilon_0$  [2], the time constant for the charge relaxation is  $\epsilon/\sigma = 3 \mu\text{s}$ . Hence, in the kHz range and lower Ohmic currents  $\sigma \vec{E}$  dominate the displacement currents  $\epsilon \frac{\partial \vec{E}}{\partial t}$ . In addition, the displacement current can lead to coupling of Faraday's and Ampère's laws resulting in electromagnetic waves. The time constant for this phenomenon  $L\sqrt{\mu_0\epsilon}$ , where  $L$  is the length scale of the object, is however an order of magnitude smaller than  $\epsilon/\sigma$ . Furthermore, if there are no external sources of the magnetic field such as rapidly-switched electromagnetic coils, also  $\partial \vec{B}/\partial t$  can be neglected in Faraday's law leading to static Maxwell's equations.

To mathematically manipulate the field equations, it is convenient to introduce the electric and magnetic fields in terms of potentials. The static electric field is curl-free and can be expressed as  $\vec{E} = -\nabla\phi$ , where  $\phi$  is the electric potential. The magnetic field is divergence-free and can be expressed using the magnetic vector potential  $\vec{A}$  as  $\vec{B} = \nabla \times \vec{A}$ . Inserting these forms into Gauss' law for  $\vec{E}$  and Ampère's law for  $\vec{B}$ , we get

$$\nabla^2 \phi = -\frac{\rho}{\epsilon_0}, \quad (2.6)$$

$$\nabla^2 \vec{A} = \mu_0 \vec{J}, \quad (2.7)$$

where the gauge  $\nabla \cdot \vec{A} = 0$  is assumed. These equations are in the form of Poisson's equation. The solution to Poisson's equation can be expressed as a convolution of the source density with the potential point source  $1/r$ , where  $r$  is the distance from the source

$$\phi = \frac{1}{4\pi\epsilon_0} \int \frac{\rho(\vec{r}')}{|\vec{r} - \vec{r}'|} dV', \quad (2.8)$$

$$\vec{A} = \frac{\mu_0}{4\pi} \int \frac{\vec{J}(\vec{r}')}{|\vec{r} - \vec{r}'|} dV', \quad (2.9)$$

where the integration domains are over all the sources. The integral solution for the electric field, i.e., Coulombs law, can now be obtained by applying gradient to Eq. (2.8) and Biot–Savart's law for the magnetic field by applying curl to Eq. (2.9):

$$\vec{B}(\vec{r}) = \frac{\mu_0}{4\pi} \int \frac{\vec{J}(\vec{r}') \times (\vec{r} - \vec{r}')}{|\vec{r} - \vec{r}'|^3} dV'. \quad (2.10)$$

## 2.2 Bioelectric and biomagnetic fields

### 2.2.1 Source currents in a volume conductor

The bioelectric and -magnetic fields originate from the active mechanisms of the nerve cells or neurons in the living body [10, 11]. In the brain, neurons communicate chemically via synapses. The redistribution of charges due to the active mechanisms in the post-synaptic neuron leads to a rising potential across the neuron membrane. Such activation is related to a local electric field that drives current in the vicinity of the cell. At macroscopic scales, this current can be modeled as an equivalent source-current density  $\vec{J}_p$  called the primary current. A single cell produces a very small primary current and it is estimated at least  $10^5$  must be activated simultaneously within a small volume in order to get a measurable biomagnetic field [2].

The active currents modeled by  $\vec{J}_p$  generate a macroscopic electric field  $\vec{E} = -\nabla\phi$  in the brain by redistributing charges at large scales. The total current density in the brain is then  $\vec{J} = \vec{J}_p - \sigma\nabla\phi$ , where  $-\sigma\nabla\phi$  is called volume current density. In the quasistatic approximation,  $\vec{J}$  is divergence-free, i.e.,  $\nabla \cdot \vec{J} = 0$ , making the field lines of  $\vec{J}$  closed loops and resulting in the following partial differential equation for the electric potential

$$\nabla \cdot (\sigma(\vec{r})\nabla\phi(\vec{r})) = \nabla \cdot \vec{J}_p(\vec{r}), \quad (2.11)$$

where  $\nabla \cdot \vec{J}_p(\vec{r})$  is interpreted as the source term.

In a uniform infinite conductor where  $\sigma(\vec{r}) = \sigma_0$ , Eq. (2.11) reduces to an ordinary Poisson's equation  $\nabla^2\phi(\vec{r}) = (1/\sigma_0)\nabla \cdot \vec{J}_p(\vec{r})$ , for which the solution can be written as

$$\phi_\infty(\vec{r}) = -\frac{1}{4\pi\sigma_0} \int \frac{\nabla \cdot \vec{J}_p(\vec{r}')}{|\vec{r} - \vec{r}'|} dV' = \frac{1}{4\pi\sigma_0} \int \vec{J}_p(\vec{r}') \cdot \nabla' \frac{1}{|\vec{r} - \vec{r}'|} dV'. \quad (2.12)$$

An analogous equation can be obtained for the magnetic field in a homogeneous conductor. By applying curl to Ampère's law (2.4), one obtains another Poisson's equation  $\nabla^2\vec{B} = \mu_0\nabla \times \vec{J}_p$ , whose solution is

$$\vec{B}_\infty(\vec{r}) = \frac{\mu_0}{4\pi} \int \frac{\nabla \times \vec{J}_p(\vec{r}')}{|\vec{r} - \vec{r}'|} dV' = \frac{\mu_0}{4\pi} \int \vec{J}_p(\vec{r}') \times \nabla' \frac{1}{|\vec{r} - \vec{r}'|} dV'. \quad (2.13)$$

To demonstrate these solutions, let us consider a simple model of the primary current density  $\vec{J}_p(\vec{r}) = J_0 \exp(-r^2/(2d^2))\hat{z}$  with a Gaussian magnitude profile illustrated in Fig. 2.1. Figure 2.1A shows the potential distribution  $\phi_\infty$  and the associated electric field lines which can be seen to originate from the sink-source pair, associated with  $\nabla \cdot \vec{J}_p$ . In Fig. 2.1B is shown the total current density, which is divergence-free. Fig. 2.1C displays the magnetic field  $\vec{B}_\infty$  following the geometry of the  $\nabla \times \vec{J}_p$ .

Far from the source, the details of a localized distribution of  $\vec{J}_p$  does not affect the field shape of  $\phi$  or  $\vec{B}$ . Then, a sufficient model for brain activity

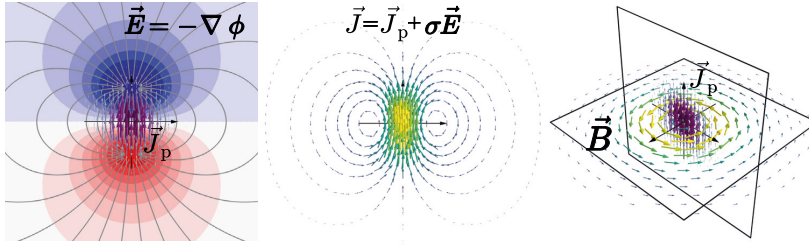


**Figure 2.1.** Fields related to a primary current density in an infinite homogeneous conductor. The primary current density is illustrated with purple arrows in the vertical plane in (A) and (C). (A) The electric potential and field lines of the corresponding electric field. (B) The total current on the same plane as (A). (C) The magnetic field depicted by the arrows on the horizontal plane.

localized in a small region can be a current dipole  $\vec{J}_p(\vec{r}) = \vec{q} \delta(\vec{r} - \vec{r}')$ , where  $\delta(\vec{r} - \vec{r}')$  is Dirac's delta function. The current dipole is a point model, which has the sink and the source of the current density at infinitesimal distance from each other.

## 2.2.2 Conductivity models and the forward problem

The infinite-conductor model may be a good model for the field in the vicinity of the sources, when the surrounding medium is approximately homogeneous. When measuring MEG and EEG, the conductivity structure of the head guides the volume currents  $-\sigma \nabla \phi$ , affecting the shapes of the magnetic and electric fields. Solving the fields affected by the volume conduction is generally known as the *forward problem*.

Because of the close-to-spherical geometry of the head, spherical head models have been used to approximate the effect of volume conduction [10]. Due to the symmetry, spherical head models exhibit some special properties, especially in MEG, manifested by easily applicable closed-form solutions.

The next simplest models are layered head-models with usually 1-4 nested compartments of homogeneous conductivity. The compartments correspond to different tissue types such as the skin, skull, cerebrospinal fluid (CSF), and the brain gray and white matter. Usually only the most distinct tissues are used for modeling the conduction effects [12, 13], while others are lumped in common compartments. The geometries of these compartments are usually obtained from structural MR images.

When using general head models, the volume conduction problem has to be solved using numerical methods such as finite-element (FEM) [13] or boundary-element methods (BEM) [14, 15]. BEMs solve the forward problem using integral equations, which are now briefly discussed.

Integral equations for the electric potential and magnetic field can be build once interface conditions for the potential and its normals derivative

between the compartments are known. As the electric field is curl free, tangential electric field is continuous across the interface and the electric potential is continuous up to a constant. Because the current density is divergence-free, the normal current on the interface must be continuous. Together these interface conditions read

$$\phi^+ = \phi^- \quad (2.14)$$

$$\sigma^+ \frac{\partial \phi^+}{\partial n} = \sigma^- \frac{\partial \phi^-}{\partial n}, \quad (2.15)$$

where the superscripts  $+$  and  $-$  refer, respectively, to the quantities on the outer and inner side of the interface.

Using the interface conditions and Green's second identity, one can derive an integral equation for the potential [16]

$$\sigma(\vec{r})\phi(\vec{r}) = \sigma_0\phi_\infty(\vec{r}) + \sum_i \frac{\sigma_i^+ - \sigma_i^-}{4\pi} \int_{S_i} \phi(\vec{r}')(\hat{n}' \cdot \nabla) \frac{1}{|\vec{r} - \vec{r}'|} dS', \quad (2.16)$$

where  $\sigma_0$  is the conductivity in the compartment containing the sources and  $\phi_\infty$  the potential in an infinite conductor Eq. (2.12). From Biot–Savart law for  $\vec{B}$ , one obtains a similar surface-integral formula for the magnetic field [17]:

$$\begin{aligned} \vec{B}(\vec{r}) &= \vec{B}_\infty(\vec{r}) + \vec{B}_v(\vec{r}, \phi), \\ \vec{B}_v(\vec{r}, \phi) &= \sum_i \frac{\mu_0(\sigma_i^+ - \sigma_i^-)}{4\pi} \int_{S_i} \frac{\hat{n} \times \nabla \phi(\vec{r}')}{|\vec{r} - \vec{r}'|} dS'. \end{aligned} \quad (2.17)$$

Both the magnetic field and the electric potential are now expressed as functions of the potential at the conductivity interfaces. The interface potentials can be solved using Eq. (2.16) by taking limits of  $\sigma(\vec{r})\phi(\vec{r})$  from inside and outside of the interfaces. Averaging the limiting values on interface  $j$ , one gets

$$\frac{\sigma_j^+ + \sigma_j^-}{2} \phi(\vec{r}) = \sigma_0\phi_\infty(\vec{r}) + \sum_i \frac{\sigma_i^+ - \sigma_i^-}{4\pi} \int_{S_i} \phi(\vec{r}')(\hat{n}' \cdot \nabla) \frac{1}{|\vec{r} - \vec{r}'|} dS'. \quad (2.18)$$

Discretizing the integral equations for all the interfaces  $j$  [14, 15],  $\phi(\vec{r})$  on the interfaces can be solved numerically.

The equations (2.16) and (2.17) seem quite similar in terms of conductivity parameters  $\sigma_i$ . However, the implicit dependence of the potential in Eq. (2.18) makes the scalp potential measured by EEG very sensitive to these parameters. On the contrary,  $\vec{B}_v$  measured by MEG is insensitive to the electric potentials outside the brain compartment, because the poorly conducting skull [18, 19] restricts the volume currents mostly in the intracranial volume. As a consequence, a good approximate volume-conductor model for the extra-cranial field is a uniform conductor bounded by the brain-skull interface [20]. A similar conclusion can be arrived at by considering the MEG forward problem from the perspective of a magnetic sensor, as done in Sec. 2.5.2.

## 2.3 Magnetization and magnetic resonance

### 2.3.1 Fields and analogy to volume-conductor problems

Although the field models in MEG utilize current densities, in MRI, it is more convenient to model the field by magnetic dipoles, elementary point-like sources of the magnetic field. The magnetic field produced by a dipole is equivalent to that of an infinitesimal current loop. Alternatively, as an analogy to electric dipoles, the field can be modeled by opposite magnetic charges or poles, separated by a small distance. The dipole is characterized by its dipole moment  $\vec{m}$ , the direction of which is perpendicular to the circulating current or parallel to the separation of the magnetic charges. A material is said to be magnetized when it contains coherently aligned magnetic dipole moments. Such material can be modeled with magnetization  $\vec{M}(\vec{r})$ , a macroscopic vector field that equals the average density of magnetic moments in a small volume around  $\vec{r}$  such that  $d\vec{m} = \vec{M}dV$ .

As the magnetic field  $\vec{B}$  is divergence-free, it cannot originate from magnetic poles. To work with the pole model, one can introduce an auxiliary magnetic field  $\vec{H}$  satisfying

$$\vec{B} = \mu_0(\vec{H} + \vec{M}). \quad (2.19)$$

In free space ( $\vec{M} = 0, \vec{J} = 0$ ),  $\vec{B}$  and  $\vec{H}$  differ only by the vacuum permeability  $\mu_0$ . When there are no free currents in the magnetic problem, one can also define the *magnetic scalar potential*  $U$  for the auxiliary field:  $\vec{H} = -\nabla U$ .

Using the definitions above, we can draw useful analogies for the magnetic field produced by  $\vec{M}$  with the fields in an infinite electric volume conductor discussed in the previous section. First, taking the divergence of Eq. (2.19), we get a Poisson equation for  $U$ :  $\nabla^2 U = \nabla \cdot \vec{M}$ , where  $\nabla \cdot \vec{M}$  can be interpreted as magnetic charge density. The potential  $U$  can be obtained as in Eq. (2.12) for the electric potential:

$$U(\vec{r}) = \frac{1}{4\pi} \int \frac{\vec{M} \cdot (\vec{r} - \vec{r}')}{|\vec{r} - \vec{r}'|^3} dV. \quad (2.20)$$

Likewise, taking the curl of Eq. (2.19), we get a Poisson equation for  $\vec{A}$ :  $\nabla \times \vec{B} = \nabla^2 \vec{A} = \mu_0 \nabla \times \vec{M}$ , where  $\nabla \times \vec{M}$  is called the magnetization current. The solution to the equation is analogous to Eq. (2.13) for the magnetic field:

$$\vec{A}(\vec{r}) = \frac{\mu_0}{4\pi} \int \frac{\vec{M} \times (\vec{r} - \vec{r}')}{|\vec{r} - \vec{r}'|^3} dV. \quad (2.21)$$

In conclusion, when  $\vec{M}$  is considered the source for  $\vec{B}$  as  $\vec{J}_p$  is for  $\vec{J}$  in an infinite volume conductor,  $U$  can be interpreted as the counterpart of the electric potential  $\sigma_0 \phi$  (Fig. 2.1A) and  $\vec{A}$  in a magnetic problem corresponds

to  $\vec{B}/\mu_0$  in a volume conductor problem (Fig. 2.1C). This also means that  $\vec{B}$  in a magnetic problem has the same role as  $\vec{J}$  in a volume-conductor problem (Fig. 2.1B), both being divergence-free.

### 2.3.2 Intrinsic magnetization in materials

In every-day magnetism, the magnetization is produced by the magnetic moments of *electrons*. Ferromagnetic materials, such as iron, contain strong magnetic interactions between the electrons, which cause the strong magnetic response of these materials as well as the remnant magnetization after the application of external fields. Materials with weaker magnetic interactions are para- or diamagnetic. In these materials, the magnetization is linearly dependent on the applied magnetic field  $\vec{M} = \chi \vec{H}$ , where  $\chi$  is the magnetic susceptibility of the material. For paramagnetic materials, the susceptibility is positive, whereas for diamagnetic materials it is negative, i.e., the effective magnetization aligns itself parallel (paramagnetic) or against (diamagnetic) the applied magnetic field.

Besides electrons, also the *nuclei* of the atoms have magnetic moments. The behaviour of nuclear magnetic moments is paramagnetic, but the resulting magnetization is 6–8 orders of magnitude smaller than in electronic paramagnetism [21]. This makes the detection of static nuclear magnetism very challenging. Instead, nuclear magnetism can be measured via magnetic resonance, where the relationship of the magnetic moments with the nuclear spins is exploited. In magnetic resonance imaging, nuclear magnetization of hydrogen is used because of its natural abundance in the human body.

### 2.3.3 Magnetic resonance

The magnetic moments of subatomic particles are related to the spin angular momentum of the particles. At microscopic level, one needs the description of quantum mechanics to handle the spins of the subatomic particles correctly. However, when the number of spins in the physical system is large and the spins only interact with macroscopic fields, the system can be described classically [22].

The magnetic moment of a system of spins with an average spin angular momentum  $\vec{S}$  is  $\vec{m} = \gamma \vec{S}$ , where the factor  $\gamma$  is called the gyromagnetic ratio. In an external field  $\vec{B}$ , a magnetic moment tends to align parallel to the field, i.e., the field applies a torque  $\vec{\tau} = \vec{m} \times \vec{B}$  on the moment. Similar to a force acting on a linear momentum (Newton's second law), the torque results in the rate of change in the total angular momentum  $\vec{L}$  as  $d\vec{L}/dt = \vec{\tau} = \vec{m} \times \vec{B}$ . In consequence, for an ensemble of particles, whose angular momentum consists only of the spins  $\vec{L} = \vec{S}$ , the magnetization

evolves according to

$$\frac{d\vec{M}(\vec{r})}{dt} = \gamma \vec{M}(\vec{r}) \times \vec{B}(\vec{r}). \quad (2.22)$$

The equation describes a rotational or *precessing* motion of  $\vec{M}$  about  $\vec{B}$  with an angular frequency  $\omega = \gamma|\vec{B}|$  called the Larmor frequency.

The general solution for this equation can be expressed in terms of a rotation matrix  $\Phi$ . With Cartesian coordinates, the right-hand side of Eq. 2.22 can be expressed as  $\omega \mathbf{C} \mathbf{m}$ , where  $\mathbf{C}$  is a unitary cross-product matrix and the column vector  $\mathbf{m}$  contains the coordinates of  $\vec{M}$ . Using the matrix exponential, the solution becomes

$$\mathbf{m} = \Phi \mathbf{m}_0 = e^{\omega t \mathbf{C}} \mathbf{m}_0, \quad (2.23)$$

where  $\mathbf{m}_0$  is the initial magnetization and  $\Phi = e^{\omega t \mathbf{C}}$ .

Assuming the magnetic field is uniform and  $z$  directional, the solution for the  $x$  and  $y$  components of the magnetization can be written as rotation in the  $xy$  plane using complex numbers. Associating the  $x$  component to the real part and  $y$  component to the imaginary part of the complex number  $\tilde{m}$ , the rotation can be described as

$$\tilde{m} = e^{i\omega t} \tilde{m}_0. \quad (2.24)$$

In a realistic physical system, spins do not only interact with the external magnetic field, but also with each other and the surrounding medium. These interactions result in relaxation, which can be modeled as two additional terms in Eq. (2.22):

$$\frac{d\vec{M}}{dt} = \gamma \vec{M} \times \vec{B} - \frac{\vec{M}_{x,y}}{T_2} - \frac{\vec{M} - \vec{M}_0}{T_1}, \quad (2.25)$$

where  $T_1$  is called the lattice relaxation time and  $T_2$  the spin-spin relaxation time, and  $\vec{M}_0$  is the equilibrium magnetization parallel to  $\vec{B}_0$ . The relaxation times are properties of materials or tissues. In MRI, they can be exploited for creating contrast between tissues with careful timing of the imaging sequence. The magnitude of the equilibrium magnetization  $M_0$  depends on the statistical properties of the spin system and is directly proportional to  $B_0$ .

The equilibrium solution to Eq. (2.25) is  $\vec{M} = \vec{M}_0$ , i.e., after several  $T_1$  relaxation times, the magnetization always returns to the equilibrium value. To start the precession, a magnetization component perpendicular to the main field is needed. In nuclear magnetic resonance, the magnetization can be perturbed from the equilibrium by an oscillating magnetic field that is in resonance with the Larmor frequency  $\gamma B_0$  and perpendicular to  $\vec{B}_0$ . According to Eq. (2.22), such oscillating field induces tipping of  $\vec{M}$  from  $\vec{M}_0$  and rotates it until the oscillating pulse is finished. In ultra-low-field MRI, the precession can also be embarked using non-adiabatic field switching [6, 23].

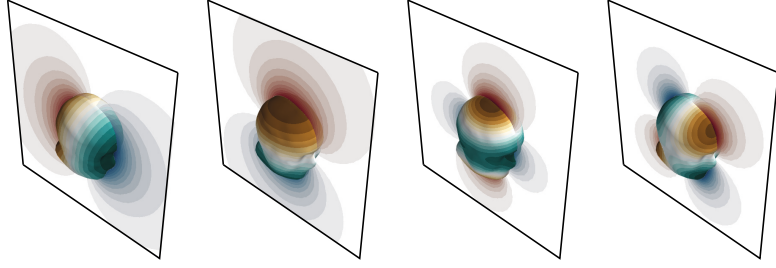


**Figure 2.2.** A few examples of surface-harmonic basis functions on a head surface and their magnetic scalar potentials. On the head surface, the green–brown colors correspond to a dipole density (stream function) which the source of the magnetic field. The blue–red colors on the vertical planes show the contours of the magnetic scalar potential. The density of the contours is proportional to the magnitude of the magnetic field.

## 2.4 Magnetic field in free space

### 2.4.1 Magnetic scalar potential

The magnetic field in a source-free space has zero curl ( $\nabla \times \vec{B} = \mu_0 \vec{J} = 0$ ). Such a field can be expressed as a gradient of a potential:  $\vec{B} = -\mu_0 \nabla U$ . To be consistent with the convention  $\vec{H} = -\nabla U$ , the vacuum permeability is included for the  $\vec{B}$  field. The scalar potential  $U$  is well-defined everywhere in simply-connected current-free regions of space [24]. As the magnetic field is also divergence-free ( $\nabla \cdot \vec{B} = 0$ ), the governing equation for the scalar potential is Laplace’s equation

$$\nabla^2 U = 0. \quad (2.26)$$

The solutions of Laplace’s equation are studied in harmonic potential theory [25], which has been applied notably in geomagnetism [26] but also in MEG [27] in terms of spherical harmonics. In the following, the representation of the magnetic field using harmonic potentials and its connection to equivalent magnetization and surface currents are discussed. More detail discussion of the application of this method can be found in Publication IV and in Ref. [28].

### 2.4.2 Equivalent sources and their decomposition

In many experimental situations magnetic measurements are made in the free space, and the magnetic sources are confined in a 3D body. As a solution to Laplace’s equation, the magnetic scalar potential is solely determined by the potential data on the bounding surface of the body [8]. Using the theory of integral equations [29] it can be shown that the

potential on the boundary can be recreated by a distribution of magnetic dipoles on the surface. In other words, an *equivalent* dipole layer can be set on the body surface and the field can be expressed as

$$U(\vec{r}) = \frac{1}{4\pi} \int_{\partial V} \psi(\vec{r}') \hat{n}' \cdot \frac{\vec{r} - \vec{r}'}{|\vec{r} - \vec{r}'|^3} dS', \quad (2.27)$$

where  $\psi$  is the magnitude of a equivalent dipole density on the surface  $\partial V$  and  $\hat{n}'$  the surface normal vector.

Similar to a single dipole that can be considered a loop of current, a surface-dipole density  $\psi \hat{n}$  is equivalent to a surface-current density. In fact, an equivalent surface current can be obtained from the dipole density as [30]

$$\vec{j}_s = \nabla_{\parallel} \psi(\vec{r}) \times \hat{n}, \quad (2.28)$$

where  $\nabla_{\parallel}$  is a gradient operator acting along the tangent planes of the surface. In this type of context, the function  $\psi$  is usually called a stream function, because the iso-contours of the  $\psi$  correspond to the stream lines of  $\vec{j}_s$ .

Because the spatial details in the magnetic field decay rapidly when moving away from the sources, it is useful to describe the field with functions that only contain low spatial frequencies. Such a representation can be obtained from Eq. (2.27) by expanding the stream function on the surface with a set of low-spatial-frequency basis functions. A suitable basis for this purpose is the eigenbasis of the Laplace–Beltrami operator  $\nabla_{\parallel} \cdot \nabla_{\parallel}$ , which generalizes sinusoidal functions to a general surface [31]. Because of this property, in Publication IV, we called these functions surface harmonics. Denoting the surface-harmonic functions as  $v_i$  the stream function can be expressed as  $\psi(\vec{r}) = \sum_i s_i v_i(\vec{r})$  and the scalar potential as where  $U_i$  is

$$\begin{aligned} U(\vec{r}) &= \sum_i s_i U_i(\vec{r}), \\ U_i(\vec{r}) &= \frac{1}{4\pi} \int_{\partial V} v_i(\vec{r}') \hat{n}' \cdot \frac{\vec{r} - \vec{r}'}{|\vec{r} - \vec{r}'|^3} dS'. \end{aligned} \quad (2.29)$$

These function and the respective potentials are illustrated in Fig. 2.2.

### 2.4.3 Relation to multipole expansion

When the surface enclosing the sources is a sphere, the eigenfunctions of the Laplace–Beltrami operator are spherical harmonics  $Y_{lm}$  and the discussed representation corresponds to the series of spherical harmonic functions, the spherical multipole expansion [27, 24]. This can be seen by expanding the inverse distance from  $\vec{r}$  to  $\vec{r}'$  in spherical coordinates  $(r, \theta, \varphi)$  as [8]

$$\frac{1}{|\vec{r} - \vec{r}'|} = \sum_{l=0}^{\infty} \frac{4\pi}{2l+1} \sum_{m=-l}^l \frac{(r')^l}{r^{l+1}} Y_{lm}^*(\theta', \varphi') Y_{lm}(\theta, \varphi). \quad (2.30)$$

Using this series and the identity  $\nabla' 1/|\vec{r} - \vec{r}'| = (\vec{r} - \vec{r}')/|\vec{r} - \vec{r}'|^3$ , the potential in Eq. (2.27) produced by an equivalent source  $\psi$  on sphere  $S$  with radius  $R$  can be expanded as

$$U(\vec{r}) = \sum_{l,m} s_{l,m} \frac{l}{2l+1} \frac{Y_{lm}(\theta, \varphi)}{(r/R)^{l+1}} = \sum_{l,m} s_{l,m} U_{l,m}(\theta, \phi), \quad (2.31)$$

where  $s_{l,m} = \int_S \psi(\vec{r}') Y_{lm}(\theta', \varphi') d\Omega'$  are the multipole coefficients corresponding to  $\psi$ . Because  $Y_l^m$  are the eigenfunctions of the Laplace-Beltrami operator, the coefficients  $s_{l,m}$  are also surface-harmonic coefficients of  $\psi$  and the functions  $U_{l,m}$  corresponds to the surface-harmonic potentials in Eq. (2.29).

Equation (2.31) is the canonical form to express all the potential configurations originating from magnetic sources inside a sphere. The potential inside a sphere due to external sources can also be expressed with spherical harmonic functions. Combining the external and internal potential, one obtains the general solution of Laplace's equation in spherical coordinates:

$$U(\vec{r}) = \sum_{l,m} \alpha_{l,m} Y_{lm}(\theta, \varphi) (r/R)^{-l-1} + \beta_{l,m} Y_{lm}(\theta, \varphi) (r/R)^l, \quad (2.32)$$

where  $\alpha_{l,m}$  and  $\beta_{l,m}$  are known as the internal and external multipole coefficients, respectively.

## 2.5 Detection of magnetic field and magnetic sources

### 2.5.1 Magnetic-field sensors

A conventional way to detect the magnetic field is to measure the electromotive force induced by a time-varying magnetic field over a coil according to Faraday's law. The detected signal is proportional to the frequency of magnetic-field signal, which makes the inductive method insensitive to lower-frequency signals such as the biomagnetic field [32]. To overcome this issue, biomagnetic signals are usually measured with superconducting quantum interference devices (SQUIDs).

The SQUID is a superconducting loop with two insulating gaps, called Josephson junctions [33]. The operation of the SQUID is based on the so-called Josephson effect and quantization of magnetic flux in a superconducting loop. Due to these effects, when the SQUID is biased with a constant current, a linear change of the magnetic flux yields a roughly sinusoidal voltage over the SQUID with a period of the flux quantum  $\Phi_0$ .

In practice, the SQUID is operated in a feedback loop with a feedback flux locking the total flux in a linear range of the periodic response curve. This setup is sensitive to the field itself and has a uniform frequency

response over a large bandwidth. Thus, coupled to a external pickup loop, the SQUID makes an excellent magnetometer for low-frequency signals. The signal measured by the device can be modeled as the instantaneous magnetic flux through the pickup loop.

For MEG, the SQUID has been the only viable sensor for a long time. However, recent developments in optics and microfabrication have enabled a new type of sensor, the optically-pumped magnetometer (OPM) [34] to emerge in MEG. This sensor does not require cryogenic environment to maintain superconductivity and can be placed much closer to the scalp than the SQUID sensors. OPM sensors use electron spin resonance of vaporized alkali-metal atoms to detect changes in the magnetic field. Instead of using magnetic field to induce precession, these devices work by lasers matched to the energy levels of the atoms. The precessing electron spins, susceptible to the external magnetic field, are also probed using a laser.

Besides OPMs, magnetometers such as giant-magneto-resistive sensors [35] and high-transition-temperature SQUIDs [36] have been aimed to be applied in biomagnetic measurements. Although these newer types of sensors can be put closer to the head, compared to conventional SQUIDs, they contain higher instrumentation noise. In consequence, SQUID-based systems are still the standard way of measuring magnetic fields from the brain. Hence, I will next concentrate on the spatial sensitivity of a SQUID coupled to a pickup loop, although the analysis would be quite similar with sensors without pickup loops.

### 2.5.2 Spatial sensitivity to magnetic sources

I will next examine how a magnetic sensor coupled to a pickup loop senses magnetic sources: the magnetization  $\vec{M}$  in MRI and primary current density  $\vec{J}_p$  in MEG. The signal, i.e., the magnetic flux over a loop surface  $S$  enclosed by the loop  $\partial S$  can be computed as

$$\Phi = \int_S \vec{B}(\vec{r}) \cdot d\vec{S} = \int_{\partial S} \vec{A}(\vec{r}) \cdot d\vec{l}. \quad (2.33)$$

For quasistatic magnetization, the vector potential is given by Eq. (2.21). By changing the order of integration, the generated flux can be written as

$$\begin{aligned} \Phi_{\vec{M}} &= \frac{\mu_0}{4\pi} \int_{\partial S} \int_{V'} \vec{M}(\vec{r}') \times \frac{\vec{r} - \vec{r}'}{|\vec{r} - \vec{r}'|^3} dV' \cdot d\vec{l} \\ &= \frac{\mu_0}{4\pi} \int_{V'} \vec{M}(\vec{r}') \cdot \int_{\partial S} \frac{\vec{r} - \vec{r}'}{|\vec{r} - \vec{r}'|^3} \times d\vec{l} dV' = \int_{V'} \vec{M}(\vec{r}') \cdot \vec{B}_s(\vec{r}') dV', \end{aligned} \quad (2.34)$$

where  $\vec{B}_s$  is the magnetic field produced by a unit current in the pickup loop. The equation for the flux can now be interpreted so that the field  $\vec{B}_s$  describes the spatial sensitivity of the pickup loop for  $\vec{M}$ . This field can be used to model the sensitivity patterns seen in (ULF) MR images [37].

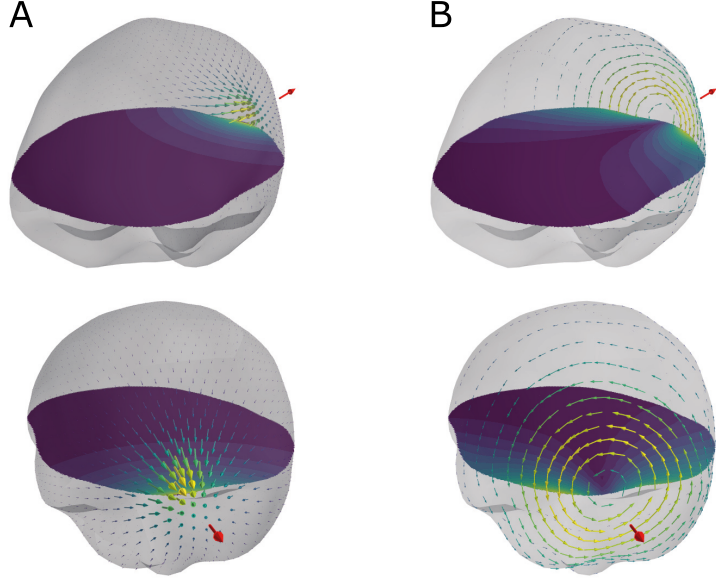


**Figure 2.3.** Sensitivity patterns of a point-like sensor (red arrow) for magnetization (A) and primary current density (B). The direction of the field is visualized on a surface representing the inner skull of the head and the field magnitude is visualized both as a color in the horizontal plane and as the color of the arrows. The sensitivity pattern for primary current is calculated assuming a homogeneous volume conductor bounded by the inner skull. The sensitivity pattern for magnetization is independent of the volume conductor.

When the magnetic flux originates from a current distribution  $\vec{J}$ , the vector potential can be expressed as in Eq. (2.9). Inserting this form in the equation for the flux and changing the order of integration, we get

$$\Phi_{\vec{J}} = \int_{V'} \vec{J}(\vec{r}') \cdot \int_{\partial S} \frac{d\vec{l}}{|\vec{r} - \vec{r}'|} dV' = \int_{V'} \vec{J}(\vec{r}') \cdot \vec{A}_s(\vec{r}') dV', \quad (2.35)$$

where  $\vec{A}_s$ , the vector potential of a unit current flowing in the pickup loop can be interpreted as the sensitivity field for  $\vec{J}$ . However, in MEG, the source of interest is not the total current  $\vec{J} = \vec{J}_p - \sigma \nabla \phi$ , but the primary current  $\vec{J}_p$ . Therefore, it is more convenient to express the flux as a linear relation with respect to  $\vec{J}_p$ .

As the total current is divergence-free, the sensitivity field  $\vec{A}_s$  is not unique, but one can add any conservative field  $\nabla U_s$  to it, so that Eq. (2.35) still holds. Denoting this field as  $\vec{L} = \vec{A}_s - \nabla U_s$  and expressing the total current as  $\vec{J} = \vec{J}_p - \sigma \nabla \phi$ , Eq. (2.35) can be written as

$$\Phi_{\vec{J}} = \int_{V'} \vec{J}_p(\vec{r}') \cdot \vec{L}(\vec{r}') dV' - \int_{V'} \sigma(\vec{r}') \nabla \phi(\vec{r}') \cdot \vec{L}(\vec{r}') dV'. \quad (2.36)$$

In Refs. [38] and [39], it is shown that the latter integral can always be made zero by choosing  $U_s$  suitably. In a piecewise-homogeneous conductor, this condition is fulfilled when  $U_s$  is harmonic in the conductive volumes and satisfies the following boundary conditions

$$\begin{aligned}\sigma_i^+ \hat{n} \cdot \nabla U_s^+ - \sigma_i^- \hat{n} \cdot \nabla U_s^- &= (\sigma_i^+ - \sigma_i^-) \hat{n} \cdot \vec{A}_s \\ U_s^+ &= U_s^-\end{aligned}\quad (2.37)$$

on each conductivity interface  $i$ . For  $\vec{L}$  that satisfies these conditions, the flux signal is simply

$$\Phi_{\vec{J}} = \int_{V'} \vec{J}_p(\vec{r}') \cdot \vec{L}(\vec{r}') dV', \quad (2.38)$$

where  $\vec{L}$  is known as the magnetic lead field. The name stems from EEG where the sensitivity of a pair leads to  $\vec{J}_p$  is proportional to the current density driven by the leads [11], i.e, the field pattern of transcranial direct current stimulation (tDCS) [40]. Similarly the magnetic lead field can be seen as the stimulation pattern of transcranial magnetic stimulation (TMS) [41].

Applying the interface conditions for the human head with high conductivity contrast between the brain and the skull, it can be seen that  $\partial U_s / \partial n \approx \hat{n} \cdot \vec{A}_s$  for  $U_s$  in the brain close to the inner skull. This means that the lead field  $\vec{L} = \vec{A}_s - \nabla U_s$  must be approximately tangential to the inner-skull boundary. Thus, when the brain tissues are lumped in a single compartment, the lead field can be calculated based on the geometry of the sensor and that of the inner skull.

Fig. 2.3 illustrates the spatial sensitivity patterns  $\vec{B}_s$  for magnetization and  $\vec{L}$  for a primary current density, assuming a point-like sensor oriented normal to the head surface. The sensitivity to magnetization is concentrated right below the sensor, while the sensitivity to primary currents picks up signal a bit off from the sensor axis. As these fields are related by  $\vec{B}_s = \nabla \times \vec{L}$ ,  $\vec{B}_s$  generally decays faster with respect to distance from the sensor compared to  $\vec{L}$ .

### 3. Background: Imaging

In this Chapter, I analyze MEG and MRI as linear imaging systems. Based on this common perspective, I use the concept of spatial response function [42] to illustrate the spatial resolution of these methods. Furthermore, I describe MEG source estimation based on additional prior information, and spatial sampling in MEG. Finally, I discuss ultra-low-field MRI, its combination with MEG, and its application to current-density imaging (CDI).

#### 3.1 Linear imaging systems

In both MRI and MEG, the magnetic measurement model is linear and can be formalized as

$$y_n = \int_V a_n(\vec{r}') s(\vec{r}') dV', \quad (3.1)$$

where  $s(\vec{r}')$  is the magnetic source and  $a_i$  are the encoding functions of the magnetic measurement  $y_i$ . The specific model for MRI is discussed in Sec. 3.2.1 and for MEG in Sec. 3.3.1.

The basic problem of imaging is to reconstruct an estimate of the source field from the measurements. If the reconstruction is linear, the estimate of the source is always a linear combination of the measurements:  $\tilde{s}(\vec{r}_m) = \sum_i w_{m,n} y_n = \mathbf{w}_m^\top \mathbf{y}$ , where  $\mathbf{w}_m$  and  $\mathbf{y}$  are column vectors of reconstruction weights and the measurements, respectively, and  $^\top$  denotes the transpose. Using Eq. (3.1), the estimate can be written as

$$\begin{aligned} \tilde{s}(\vec{r}_m) &= \sum_i w_{m,n} \int_V a_n(\vec{r}') s(\vec{r}') dV' = \\ &= \int_V \left( \sum_n w_{m,n} a_n(\vec{r}') \right) s(\vec{r}') dV' = \int_V v_m(\vec{r}') s(\vec{r}') dV', \end{aligned} \quad (3.2)$$

where  $v_m(\vec{r}) = \sum_n w_{m,n} a_n(\vec{r})$  is the *spatial response function* (SRF) [42] of the image element at  $\vec{r}_m$ . In other contexts, the SRF is known as the

averaging kernel [43], the resolution field [44] and the cross-talk function [45] with subtle differences in their definitions. The SRF describes the sensitivity of the image value, e.g., a pixel value to the source distribution surrounding  $\vec{r}_m$ . In the optimal case, the SRF corresponds to Dirac's delta function  $v_m(\vec{r}) = \delta(\vec{r}_m - \vec{r})$  so that  $\hat{s}(\vec{r}_m) = s(\vec{r}_m)$ .

To find an optimal local estimate for  $s(\vec{r})$  within the constraints of the imaging modality, one can optimize the weights so that the difference  $\|v_m(\vec{r}) - \delta(\vec{r} - \vec{r}_m)\|^2$  measured by the  $L_2$  norm is minimized. In terms of the weights  $w_m$ , the optimization problem becomes

$$\min_{w_m} w_m^\top G w_m - 2w_m^\top a_m, \quad (3.3)$$

where  $G$  is a Gram matrix with elements  $G_{nm} = \int_V a_n(\vec{r}) a_m(\vec{r}) dV$  and  $a_m$  contains the basis function values at  $\vec{r}_m$ :  $(a_m)_n = \int \delta(\vec{r} - \vec{r}_m) a_n(\vec{r}) dV = a_n(\vec{r}_m)$ . The solution to this minimization problem can be found by equating the gradient of the objective function to zero, which gives

$$w_m = G^{-1} a_m. \quad (3.4)$$

Unless the basis functions are orthonormal with respect to the inner product, i.e.,  $G = I$ , the solution may become unstable. This can be alleviated by penalizing for the expected squared error of the source estimate in the objective function. If the measurements  $y$  contain additive noise with a covariance matrix  $C$ , the expected squared error in  $\tilde{s}(\vec{r}_m)$  is  $w_m^\top C w_m$ . By adding this quadratic form multiplied by a trade-off parameter  $\lambda$  to the objective in Eq. (3.3), the minimization of the objective yields a regularized solution

$$w_m = (G + \lambda C)^{-1} a_m. \quad (3.5)$$

The spatial resolution of a linear imaging modality can be obtained from the SRF. For demonstration, I now use complex sinusoidal functions  $e^{ikx}$  to build a SRF, motivated by the fact that these are the encoding functions in the most basic form of MRI. For simplicity, let us assume a one-dimensional domain of a length  $L$ ; the SRF generalizes to 2D and 3D rectangular domains as a product of the 1D SRFs of each coordinate. The basis functions  $a_n = e^{ik_n x}$  are orthogonal in the domain, when  $k_n = 2\pi n/L$ , i.e.,  $G = LI$ . According to Eq. (3.4), the optimal weights for a point at  $x = x_m$  are then  $(w_m)_n = a_n(x_m) = e^{ik_n x_m}/L$  and the corresponding SRF is

$$v_m(x) = \frac{1}{L} \sum_{n=-N}^N e^{ik_n(x-x_m)} = \frac{\sin\left(\frac{2\pi}{L}(N+1/2)(x-x_m)\right)}{L \sin\left(\frac{2\pi}{L}(x-x_m)/2\right)}, \quad (3.6)$$

which is called the Dirichlet kernel, illustrated in Fig. 3.1A. One possible way to define the spatial resolution of the imaging system is the width of the main lobe of the SRF. This width is inversely proportional to the highest measured spatial frequency  $k_N$ .

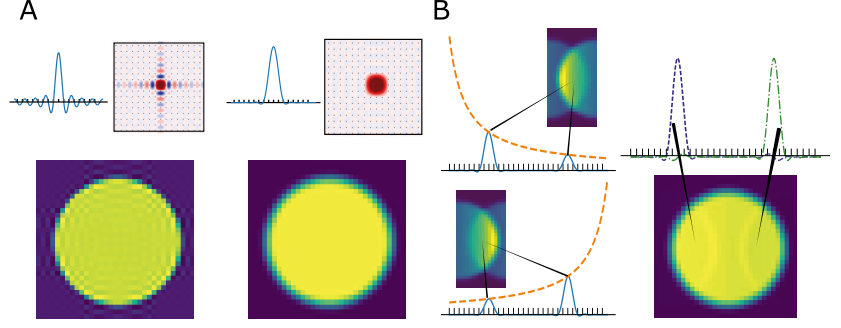


**Figure 3.1.** Spatial response functions in MRI. **A:** On the left, the Dirichlet SRF in 1D, and in 2D as well as a simulated MR image of a disc corresponding to the SRF. On the right, the SRF of Hann-windowed  $\vec{k}$  space data as well as the corresponding reconstruction of the disc. **B:** On the left, two SRFs of undersampled multichannel imaging (blue lines) for two different channels and the corresponding images spatially aliased in the horizontal direction. The orange envelope curves visualize the spatial sensitivity profiles of the two channels. On the right, the two SRFs are resolved as weighted combinations of the SRFs on the left using the SENSE method.

Although the SRF is optimal in the sense of squared error, it may not be optimal with respect to other criteria. For example, the Dirichlet kernel contains far-reaching side lobes, i.e., the estimate  $\tilde{s}(x_m)$  can pickup source signal far from  $x_m$ , which can cause ringing artifacts in the image (see Fig. 3.1A). To reduce the side lobes, one can damp the terms corresponding to the higher spatial frequencies, the trade-off being that the main lobe widens. Different measures the optimality are discussed by Backus and Gilbert in Ref. [43], where the SRF is known as the averaging kernel.

## 3.2 MRI

### 3.2.1 Encoding and reconstruction

As explained in Sec. 2.3.3, when tipped from equilibrium, nuclear magnetization  $\vec{M}(\vec{r})$  precesses around the external magnetic field with the angular frequency  $\omega = \gamma B$ . When expressing the precessing magnetization in the  $xy$  plane as a complex number as in Eq. (2.24), the model for the detected, magnetic flux in Eq. (2.34) can be written in the form of a linear measurement (Eq. (3.1))

$$\Phi(t) = \text{Re} \int_V \beta(\vec{r})^* e^{-i\phi(\vec{r},t)} \tilde{m}_0(\vec{r}) dV, \quad (3.7)$$

where  $\beta = B_{s,x} + iB_{s,y}$  is obtained from the sensitivity field  $\vec{B}_s$ . Here,  $\tilde{m}_0(\vec{r})$  is the magnetization, i.e., imaged source and  $\beta(\vec{r})^* e^{-i\phi(\vec{r},t)}$  is the

encoding function, which depends on the phase of the magnetization  $\phi(\vec{r}, t) = \int_0^t \omega(\vec{r}, t') dt'$  as well as on the sensor location.

Magnetic resonance imaging is based on manipulating the magnetization phase across the imaged volume. By varying the phase linearly  $\Delta\phi(\vec{r}) = \vec{k} \cdot \vec{r}$ , the exponential part of the encoding functions become Fourier basis functions  $e^{i\vec{k} \cdot \vec{r}}$  and Fourier transform can be used to efficiently reconstruct the image. The linear phase change is achieved by introducing so-called gradient fields  $\vec{B}_g$  on top of the main field. When  $B_0 \gg B_g$  and  $\vec{B}_0$  is  $z$  directional, the variation in the field magnitude is approximately  $\vec{B}_g \cdot \hat{z}$ . Choosing  $\vec{B}_g$  such that  $\vec{B}_g(\vec{r}) \cdot \hat{z} = \vec{G} \cdot \vec{r}$ , linear phase encoding is achieved.

In practice, the gradient sequence consists of two steps: phase and frequency encoding. Phase encoding varies the phase before the signal acquisition and frequency encoding varies it during the acquisition. The purpose of these two steps is to gather data that corresponds to basis functions with different  $\vec{k}$  vectors:

$$y(\vec{k}_n) = \int_V \beta(\vec{r})^* \tilde{m}_0(\vec{r}) e^{-i\vec{k}_n \cdot \vec{r}} dV, \quad (3.8)$$

The collection of samples then constitutes a data array which can be interpreted as samples of the Fourier transform of  $\beta^*(\vec{r})\tilde{m}(\vec{r})$  in the reciprocal  $\vec{k}$  space. In conventional Fourier imaging, the  $\vec{k}$  space is sampled uniformly using a series of phase- and frequency-encoding steps.

A linear reconstruction of the source can be obtained by optimizing the spatial response function for chosen source locations [42]. If  $\beta^*(\vec{r})\tilde{m}(\vec{r})$  is considered as the image (instead of  $\tilde{m}(\vec{r})$ ), the encoding functions are of the form  $e^{i\vec{k} \cdot \vec{r}}$  and the optimal reconstruction corresponds to the SRF optimization in Sec. 3.1. When the image is reconstructed in a pixel- or voxel-based manner, values are required only for points in a regular grid and the reconstruction weights become the elements in a discrete Fourier transform (DFT) [42]. The reconstruction to a regular grid can thus be carried out by the efficient Fast-Fourier-Transform algorithm (FFT). Finally, the voxel values can be corrected for the sensitivity profiles by dividing the reconstructed values by  $\beta^*(\vec{r})$ .

Although this is the usual way of reconstructing an MR image, the estimated values of the source  $\beta^*(\vec{r})$  are not restricted to the grid points determined by the DFT. The optimal reconstruction to the points between the DFT grid can be obtained efficiently by the FFT by zero-padding the  $\vec{k}$  space data. Extending the zero padding, the optimal continuous reconstruction of the source is approached.

### 3.2.2 Multi-channel MRI

In many MRI applications, the magnetic field generated by precessing nuclear magnetization is received by multiple sensors positioned around the imaged object. Each sensor  $j$  forms a channel that gathers the signal

from the source weighted by its own sensitivity profile  $\beta = \beta_j$  as described in Eq. (3.7). Assuming the FFT-reconstruction yields spatial response functions sufficiently close to a delta function, FFT can be applied sensor-wise to reconstruct single-channel images  $\beta_j^*(\vec{r})\tilde{m}(\vec{r})$ . These images can be combined voxelwise as a weighted sum of the voxel values in each image to obtain the imaged of  $\tilde{m}(\vec{r})$  [37].

When considering  $\beta_j(\vec{r})e^{-i\phi(\vec{r},t)}$  Eq. (3.7) as the encoding functions, one is not limited to the conventional  $\vec{k}$  space imaging, but can also use the encoding power of the sensitivity profiles  $\beta_j(\vec{r})$ . Such generalized encoding can be used to reduce the number of data acquisitions, which decreases the total imaging time. The most convenient way to do this is to under-sample the  $\vec{k}$  space along the phase encoding dimensions. For instance, undersampling by a factor 2 in two dimensions, reduces the imaging time to one fourth.

When using the FFT-based reconstruction, the undersampling leads to aliasing or folding of the image on top of itself, which can be understood in terms of the spatial response function. The SRF of FFT reconstruction, described by Eq. (3.6), is periodic with a period of  $L = 1/\Delta k$ , where  $\Delta k$  is the sampling interval in the  $\vec{k}$  space. Because the SRF peaks at every period, features at the period of  $L$  will sum up to the same voxel and folding occurs if  $L$  is smaller than the object size. The folding can be resolved when the image data is captured by multiple sensors. One such method is called SENSE (sensitivity encoding) [46], which works by solving the linear equations associated with the aliased sensitivity profiles  $\beta_j(\vec{r})$ . Because the sensitivity profiles decay and smooth out with distance from the sensor, resolving the aliasing works best at the superficial parts of the head [47].

### 3.3 MEG

#### 3.3.1 Minimum norm estimate

In magnetoencephalography, the linear model for the measurements can be formulated using the lead fields in Eq. (2.38). For each sensor the model for the data is then simply

$$y_n = \int_V \vec{L}_n(\vec{r}) \cdot \vec{J}_p(\vec{r}) dV, \quad (3.9)$$

where  $\vec{L}_n$  is the magnetic lead field of the sensor  $n$ . When compared to multi-channel MRI, the model would roughly correspond to having data without any gradient encoding. Mirrored by this fact, one could estimate that MEG, as an imaging modality, has a very limited spatial resolution compared to MRI.

The resolution of MEG can be quantified using the spatial response

function, which in this context is a vector field called the resolution field [44, 48]. A similar concept is the cross-talk function [45], which is usually only considered in a discretized setting. The optimal reconstruction weights derived using Eq. (3.4) for source location  $\vec{r}_m$  are

$$\vec{w}_{m,n} = \sum_k (\mathbf{G}^{-1})_{n,k} \vec{L}_k(\vec{r}_m), \quad (3.10)$$

and the corresponding SRF is

$$\vec{\vec{R}}_m(\vec{r}) = \sum_{n,k} (\mathbf{G}^{-1})_{n,k} \vec{L}_k(\vec{r}_m) \vec{L}_n(\vec{r}), \quad (3.11)$$

where  $G_{n,k} = \int_V \vec{L}_n(\vec{r}) \cdot \vec{L}_k(\vec{r})$  and the double vector denotes a second-order tensor. The corresponding estimate  $\vec{J}_{MN}(\vec{r}_m) = \sum_n \vec{w}_{m,n} y_n$  is known as the minimum-norm estimate. Since the lead fields are not orthogonal, the inversion of the matrix  $\mathbf{G}$  is generally not stable. Therefore, the estimate is usually *regularized* by replacing  $\mathbf{G}$  with  $\mathbf{G} + \lambda \mathbf{C}$  as in Eq. (3.5).

Fig. 3.2 shows examples of the SRF for two current estimates computed using an inner-skull-based single-compartment head model. Since the lead fields are divergence-free and tangential on the conductivity interface, so is the resolution field. These examples explain visually the sensitivity of MEG to superficial source activity. Although the SRF can be optimized for deeper source activity, it always picks up activity primarily from the superficial parts of the brain, if such activity is present.

### 3.3.2 Source estimation using additional prior information

In order to make inference of the brain activity based on magnetic-field measurements, one must have prior knowledge of how the field is generated. In a broad sense, this prior knowledge includes the geometry of the sensor arrangement, the geometry of the head conductivity structure, conductivity parameters, i.e., the whole forward model. Error in any part of the model may affect accuracy of the estimate of the source activity.

In a more strict sense, the prior knowledge only refers the source currents  $\vec{J}_p(\vec{r})$  and other parts of the physical model are considered to be certain. One can then assign prior probabilities for  $\vec{J}_p(\vec{r})$  according to one's beliefs of where the activity can take place. A common prior assumption is that the source activity lies normal to the surface of the cortex, in the direction of pyramidal neurons [2, 49]. This assumption constrains the minimum-norm estimate to the cortex. However, as the cortex is highly folded the estimate can spread over multiple sulci [49, 50].

In some situations, one can expect to have the source activity primarily concentrated on certain focal locations. When only one dominating location is assumed, it can be searched by dipole fitting, i.e., by varying location and orientation of a candidate dipole and matching the field topography of

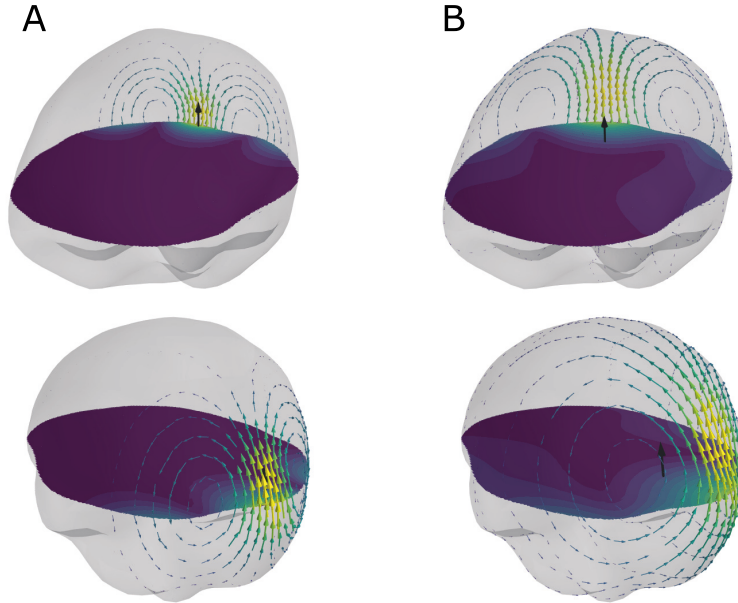


**Figure 3.2.** Spatial response functions (SRFs) for estimates of  $\vec{J}_p$  pointing upwards at two locations. **A:** Superficial location at 4 mm from the inner skull. **B:** Deeper location at 4 cm from the inner skull. The field magnitude and direction are plotted on the inner skull surface. The field magnitude is shown also on the horizontal plane. The SRF for the superficial location is quite well-concentrated around the desired location, but the SRF for the deeper location is biased towards the more superficial areas.

the dipole with the measured one. When multiple active locations are assumed, one may use multiple-signal classification (MUSIC), beamformers [10], or Bayesian multi-dipole methods [51] to determine these locations. Beamformers can also be interpreted as spatial filters [52], which can be analyzed using spatial response functions (cross-talk functions [45]). Instead of building the reconstruction weights only based on the field model ( $\vec{L}$ ) as in MNE, beamformers also use data over the whole time course.

The methods described above try to resolve the neural activity in greater detail than than minimum-norm estimation by taking advantage of small differences in the field topographies. As a consequence, they require more accurate modeling of the electromagnetic field. In MEG, a major issue can be the errors in spatially aligning head model with the MEG sensors [53, 54, 55], which distort the forward model. Although in EEG, uncertainties in the conductivity structure of the head play a big role [56, 57], in MEG they have only minor effect [12, 58].

### 3.3.3 Spatial sampling

In conventional MRI, the signal is sampled in the  $\vec{k}$  space, and the effect of sampling, such as aliasing of the image, can be studied with conventional methods of signal processing. In MEG, the field signal is only sampled in the real space with sensors placed around the head. Adequate sampling of the magnetic field is needed to get the full picture of the continuous field profile. Modern MEG devices contain hundreds of magnetic sensors sampling the field and it has been argued that they provide substantial oversampling of the field [59, 27]. With the coming of new types of sensors (Sec. 2.5.1) that can be flexibly positioned, the sampling issue has also become more and more relevant.

The sampling in MEG has been thoroughly analyzed in terms of spatial frequencies [59] and aliasing of the signal in the Fourier ( $\vec{k}$ ) space. The analysis works well in flat domains but remains only an approximation of the realistic situation, where the sensors are positioned on a curved surface. In Publication III, it was demonstrated that similar analysis can be made on a surface, when the Fourier basis functions are generalized as eigenfunctions of the Laplace–Beltrami operator. Although there is no similar notion of  $\vec{k}$  as in flat 2D domains and conventional sampling analysis cannot be done, the number of basis functions needed to represent the magnetic field patterns of the brain can be used to estimate the number of samples required.

Another problem is how to position or orient the sensors when the number of sensors is fixed. When assuming homogeneous uncorrelated activity within the brain, the goodness of the sampling configurations can be quantified by calculating the total information or the channel capacity [60, 61]. Under this assumption, the total information (TI) is a function of the Gram matrix  $\mathbf{G}$  used in the minimum norm estimate (Eq. (3.11)) and the noise covariance matrix  $\mathbf{C}$ :

$$\text{TI} = \frac{1}{2} \log_2 \frac{\det(q^2 \mathbf{G} + \mathbf{C})}{\det(\mathbf{C})}, \quad (3.12)$$

where  $q^2$  is the assumed variance of  $\vec{J}_p$  within the brain.

The optimal sampling configuration depends on the prior assumptions of the brain activity encoded in the matrix  $q^2 \mathbf{G}$ . Furthermore, if external field fluctuations exist, they create measurement noise that correlates between the sampling locations, and it should be taken into account in the noise covariance  $\mathbf{C}$ .

### 3.4 Ultra-low-field MRI and MEG–MRI

#### 3.4.1 Basics principles of ultra-low-field MRI

The strength of the main field of conventional MRI is 1–7 T, and even higher field strengths are strived for. The need for high field strengths exists mainly because the main field is used for magnetizing the spin population and higher magnetization gives better quality signal. On the contrary, in ultra-low-field MRI, the main field strength is in the order of the Earth's magnetic field, 50  $\mu$ T, [5, 6] and the corresponding Larmor frequency is around 2 kHz. The low main field is not enough to build up required magnetization. Therefore, prepolarization, i.e., a strong field pulse of 10–100 mT is applied before the signal encoding and acquisition. Such a strong pulse creates eddy-current problems, which have to be dealt with using special techniques [62, 63].

Prepolarization itself does not enable imaging at ultra low fields. Another problem is the acquisition of MR signals of low Larmor frequency, since, as described in Sec. 2.5.1, inductive measurement of the magnetic field loses sensitivity at low frequencies. As in MEG, this problem is solved by using SQUID sensors, that provide a flat response in the frequency range of ULF MRI. However, the SQUIDS must bear high prepolarization pulses and they must be designed more carefully than the ones aimed only for MEG [64, 65].

After taking care of instrumentation problems, ULF MRI has unique possibilities for biomagnetic measurements. First, a multi-sensor system capable of measuring ULF MRI can be directly used for MEG studies. Additionally, ULF MRI itself has several advantages compared to high field MRI. At low fields, the magnetization relaxation times change compared to high fields, enabling improved image contrast for certain tissues [66, 67, 68]. Furthermore lower fields enable more flexible design of imaging sequences [69, 23], e.g., a sequence for three-dimensional current-density imaging discussed in more detail below.

However, there are several challenges, e.g, low SNR and long prepolarization times [70], which limit to the achievable spatial resolution of ULF MRI. Additionally, one major physical hindrance are the so-called concomitant gradients, i.e., the orthogonal components of the gradient field  $\vec{B}_g$  [71]. Because  $\vec{B}_g$  is a gradient of a harmonic potential (Sec. 2.4.1), such a component is always present at some part of the imaging volume. At low fields the orthogonal components contribute to the field strength approximately as [72]

$$|\vec{B}_0 + \vec{B}_g| \approx (B_0 + \vec{B}_g \cdot \hat{z}) \left( 1 + \frac{|\vec{B}_g^\perp|^2}{2(B_0 + \vec{B}_g \cdot \hat{z})^2} \right), \quad (3.13)$$

where  $\vec{B}_g^\perp$  is the concomitant component. When  $B_g$  approaches  $B_0$  in any part of the image, the encoded phase becomes non-linear with respect to location, i.e.,  $\phi \neq \vec{k} \cdot \vec{r}$  and the notion of  $\vec{k}$  space loses its meaning. On the other hand, imaging with lower gradients requires longer encoding times, resulting in relaxed magnetization and smaller signals.

To a certain extent, the concomitant effect can be handled as a geometric distortion when using a FFT reconstruction [72]. The image can also be reconstructed by explicitly modeling the encoding functions affected by the concomitant fields [73], but the reconstruction involves matrix inversions, which takes more time and can be more susceptible to modeling errors.

### 3.4.2 Current-density imaging

In MRI, any inhomogeneity on top of the main  $B_0$  field causes the precessing magnetization to dephase. This effect is exploited to spatially encode the magnetization by gradient fields. Any additional field causes additional phase change which can be quantified by the phase of the complex voxel values. One such field is the one generated by current density in the brain  $\vec{B}_J$ . If the source of the current density is the brain, as in MEG, the imaging modality is called neuronal current imaging (NCI) [74]. It has been estimated that the strength of the local field generated by a local activation can be in the order of 1 nT [75, 76]. If the field is in the direction of  $\vec{B}_0$ , the related phase change in  $\tau = 100$  ms (a typical relaxation time of ULF-MR signal) is only  $\Delta\phi = \gamma\tau B_J = 1.5^\circ$ . For a detectable NCI signal, a high signal-to-noise ratio and a long-lasting activation are needed.

Instead of relying on fields generated by the brain, one can use externally *injected* currents to study current distributions in the head. The effect of  $\vec{B}_J$  on the MR signal can be more easily controlled by the amplitude and duration of the applied current. In high-field MRI, the detection of injected currents is mainly limited to recording the component of  $\vec{B}_J$  parallel to  $\vec{B}_0$  [77] and such measurements are of limited use. However, the flexibility in the sequence design of ULF MRI enables measuring all three components of  $\vec{B}_J$  [78, 23], which can be used to fully resolve the underlying  $\vec{J}$  field by the application of Ampère's law. Direct imaging of  $\vec{J}$  can offer valuable information about the conductivity structure of the head.

The encoding of  $\vec{B}_J$  into the MR signal is based on a zero-field sequence, where the main field is switched off after the prepolarizing pulse, before the spatial encoding. During the zero-field time, the magnetization rotates around  $\vec{B}_J$  according to Eq. (2.23), illustrated in Fig. 3.3. Switching on  $\vec{B}_0$  and continuing with conventional spatial encoding, one can measure projection of the rotated starting magnetization in the  $xy$  plane perpendicular to  $\vec{B}_0$ . When the measurement is repeated for three orthogonal starting magnetizations, the projections of these vectors can be used to determine the associated rotation matrix  $\exp(\phi(\vec{B}_J)\mathbf{C}(\vec{B}_J))$ , which contains

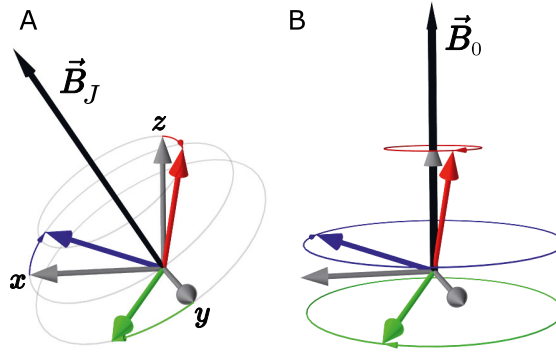


**Figure 3.3.** Rotation of the orthogonal starting magnetizations (blue, green, and red arrows) initially oriented along the coordinate axis in zero-field encoded CDI sequence. **A:** Application of  $\vec{B}_J$  during the zero-field period rotates the starting magnetization vectors. **B** After the application of  $\vec{B}_0$  the rotated vectors start to precess around  $\vec{B}_0$ . The  $x$  and  $y$  components of the rotated vectors contribute to the MR signal from which they can be resolved for each voxel in the image.

the information for reconstructing  $\vec{B}_J$ .

Although current-density imaging has been successfully demonstrated in a homogeneous phantom [23], applying the technique for humans has several complications, discussed in Publication II. First, the applied current is limited to approximately below 4 mA to prevent uncomfortable sensations in the skin [79]. Second, the human head is not homogeneous in conductivity, but the relatively resistive skull hinders the current transmitted into the brain [80], lowering the SNR of intracranial CDI. Another problem is the inhomogeneity of the magnetization in the different tissue types. Since the skull has effectively no magnetization,  $\vec{B}_J$  cannot be measured there either. A voxel positioned at the skull actually measures  $\vec{B}_J$  from the neighbouring areas based on its spatial response function.

### 3.4.3 Co-registration and Spatial Calibration of MEG and MRI

The use of detailed prior information in MEG discussed in Sec. 3.3.2 requires accurate forward modeling. Since the conductor model for MEG does not require to be very detailed, the major errors in the physical model usually come from the spatial alignment, i.e., the co-registration of MEG sensors and the geometrical model of the head. The MRI-derived head model comprises the conductivity boundaries for modeling the volume conduction and possibly the cortex for constraining the inverse solution. The co-registration problem is a major issue both in the workflow of MEG experiments, but also in the processing of MEG data. It involves manual steps, which can be susceptible to human errors [81].

A typical co-registration procedure involves multiple coordinate systems, in which the data are presented [82]. One of these is the *MRI coordinate*

*system* describing structural MR data as voxel values in a rectangular grid. Depending on the MR device and the imaging sequence, the geometry of the head can already be distorted in this coordinate system. The geometrical model of the head derived from the MR images must be positioned in the *MEG coordinate system*, i.e., the coordinate system of the MEG sensors, to derive the physical field model ( $\vec{L}$ ). This is usually accomplished with a 3D digitizing device, which maps positions on the head in its own *head coordinate system*. Certain digitized positions are then localized in MEG coordinate system with the help of small energized coils whose signal is measured by the MEG sensors. Additionally, a larger set of digitized positions are used to map the MRI-based head model in the head coordinate system. Finally, after the two coordinate transformations determined from this procedure, the geometrical model of the head can be positioned with respect to the MEG device.

In combined MEG–MRI, the co-registration procedure is somewhat simpler as these manual steps can be avoided. The MEG and ULF-MR coordinate systems can be spatially calibrated without relation to a head coordinate system as described in Publication I. Therefore, when data from both modalities are recorded in the same session and the head stays still, ULF-MR data such as structural or current-density information can be obtained in the same coordinates as MEG. Structural ULF-MR data can also be co-registered with structural high-field MR data [83], enabling automatized use of high-field MR data, e.g., for MEG source modeling.

## 4. Summary of Publications

### 4.1 Publication I: "Automatic spatial calibration of ultra-low-field MRI for high-accuracy hybrid MEG–MRI"

As described in Sec. 3.4.3, the co-registration of MR images and the MEG device is laborious and prone to errors. In this publication, we approached the co-registration problem from a different perspective, in the context of a hybrid MEG–MRI device. Instead of using conventional co-registration procedures, the device can be spatially *calibrated* so that every ULF-MR image taken with device can be accurately expressed in the MEG coordinates (see Fig. 4.1).

We developed a spatial calibration method that uses the spatial information in the MR sensitivity profiles  $\beta_j$  described in Secs. 2.5.2 and 3.2.1. This method solves the placement of the ULF-MR image with respect to the magnetic sensors using single-channel images of a phantom and a computational model for the spatial sensitivities  $\beta_j$ . With extensive computer simulations, we verified the feasibility of the method in high-noise conditions and demonstrated that it can reach sub-voxel and sub-millimeter accuracy in the spatial calibration. The method ensures the enhanced spatial accuracy in the co-registration of MRI and MEG when using the MEG–MRI device.

### 4.2 Publication II: "Evaluating the performance of ultra-low-field MRI for in-vivo 3D current density imaging of the human head"

Ultra-low-field MRI can be applied for imaging currents (CDI) injected into the head as described in 3.4.2. In order to reconstruct the currents from the MR image data, one needs high-enough signal-to-noise ratio (SNR). The purpose of this study was to quantify the SNR of magnetic-field ( $\vec{B}_f$ ) and current-density ( $\vec{J}$ ) reconstructions in terms of image SNR, which is

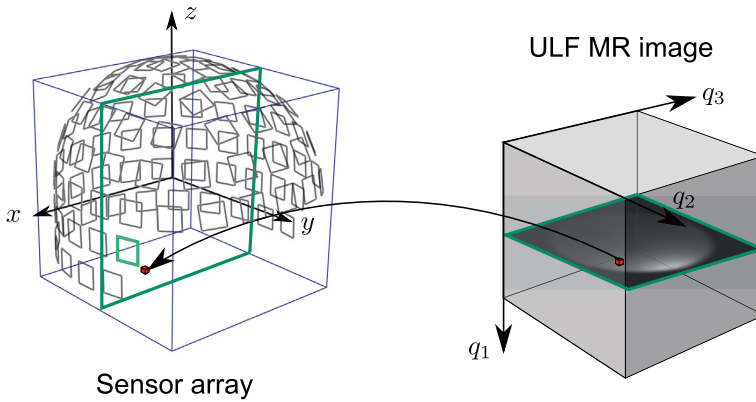


**Figure 4.1.** The spatial calibration method in Publication I finds the location of the MRI image voxels (e.g. the red cube) in the coordinate system of the sensor array. The locations are determined by a fitting a mapping between the coordinate system of the sensor array  $(x, y, z)$  and the coordinate system of the ULF MR image  $(q_1, q_2, q_3)$ .

easier to estimate. We also carried out simulations of  $\vec{J}$  and  $\vec{B}_J$  (Fig. 4.2) using a realistically shaped three-compartment head model and a finite-element method. By incorporating the field simulations in an accurately modelled zero-field encoded CDI sequence, we determined whether the SNR would be high-enough in two existing ULF-MRI systems for in-vivo measurements. One of the systems was the multichannel MEG–MRI system at Aalto University and the other one was a one-channel system at PTB Berlin.

Based on this computational study, the magnetic field  $\vec{B}_J$  generated by the current density  $\vec{J}$  can be reconstructed reasonably well in the intracranial volume near the skull in both systems. However, the current-density reconstructions were more susceptible to image artifacts that originate from the scalp-skull structure and the SRF sidelobes. The elimination of these artifacts should still be studied more thoroughly.

#### 4.3 Publication III: "Spatial sampling of MEG and EEG revisited: From spatial-frequency spectra to model-informed sampling"

In this study, spatial sampling of continuous field patterns generated by the brain was analyzed. Based on a spatial-frequency analysis conveyed using Laplace–Beltrami eigenfunctions, the number of sensors that sufficiently sample all the possible field patterns was estimated. For field samples positioned on around 2 cm away from the scalp, this number was around 100 which corresponds to the number of magnetometers in the new prototype of the MEG–MRI device at Aalto University. Thus, the

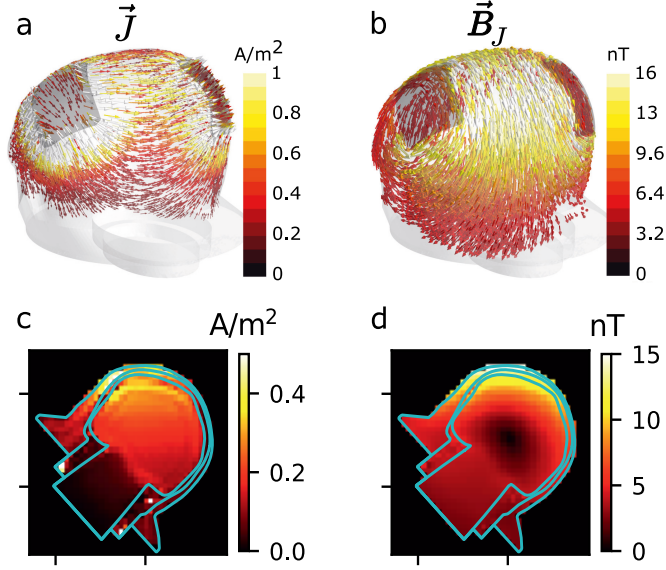


**Figure 4.2.** The current density  $\vec{J}$  and magnetic field  $\vec{B}_J$  solved with a finite-element method and used in the CDI simulations of Publication II are shown in panels **a** and **b**. Panels **c** and **d** show the magnitude of the field reconstructions derived from the simulated MR data. In these examples, no noise was applied to the simulation to show the artifacts in the reconstruction of current density  $\vec{J}$ .

300 sensors equipped in conventional MEG devices are overly sufficient for sampling of MEG, although they may be beneficial in other respects, e.g., in interference detection. We also carried out the same analysis for on-scalp MEG and EEG. For MEG sensors that can be positioned on the scalp, the beneficial number of sensors was around 300 and for EEG it was approximately 100.

We applied the theory of Gaussian processes and optimal design (see Fig. 4.3) to analyze how sensor positioning affects the total information (Eq. (3.12)) conveyed from the brain. Furthermore, we developed a method to design sampling configurations that are optimal in this respect. The information metric was compared among different sampling configurations for two different cases of prior information: uniform activation around the brain and an activation located in a certain region of interest. The optimized sampling positions were especially useful for the latter case. In future, the sampling method may be applied in studies where a certain region of brain is known to be activated and the sensors can be freely positioned.

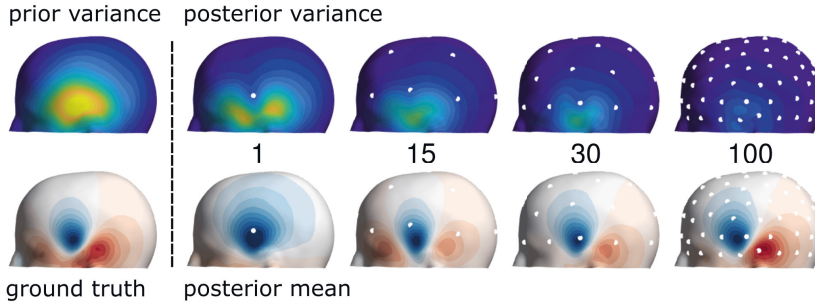


**Figure 4.3.** Prior variance encodes the uncertainty of the field based on a prior model set by the experimenter before measurements. Using Bayesian inference, the uncertainty after measurements (posterior variance) can be calculated. The posterior mean is the expected field pattern incorporating information from the prior model and the measured field samples. The figure illustrates the posterior mean and variance for 1, 15, 30, and 100 uniformly distributed samples. The more samples, the less uncertainty is left in the field and the more accurate estimate is the posterior mean for the ground truth.

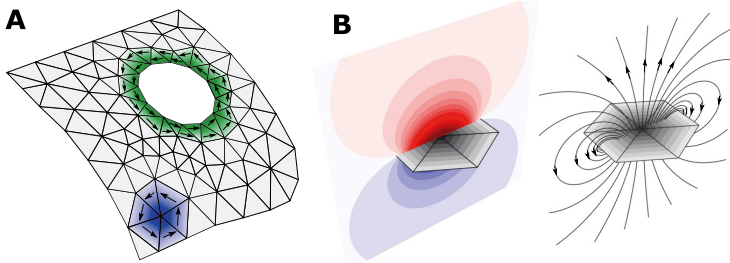


**Figure 4.4.** Panel **A**: An example of triangle mesh used in the field modeling in Publication IV. Blue and green color indicate the magnitude of two basis functions on the surface. The basis functions can be used to describe basis current densities (black arrows), which circulate either the nodes or holes of the mesh. Panel **B**: The magnetic scalar potential on the left and the magnetic field on the right originating from a single basis-function current. The different shades of grey on the triangles represent the magnitude of the stream function.

#### 4.4 Publication IV: "Magnetic-field modeling with surface currents. Part I. Physical and computational principles of bfieldtools"

In this study, we designed and implemented general computational tools for modeling quasistatic magnetic fields. The tool set is primarily based on representing the magnetic field using divergence-free surface currents (Sec. 2.4). The computations were aimed for arbitrary surface-current geometries by discretizing the stream function of the current density using triangle meshes. The field equations associated with the stream function were analytically discretized for accurate computations as shown in Fig. 4.4. Additionally, the construction of function bases for field processing using the Laplace–Beltrami eigenfunctions was implemented.

The tools described in this work are currently available as a software

package called `bfieldtools` in a public code repository available at <https://github.com/bfieldtools/bfieldtools>. This package can be used for a variety of tasks from eddy current problems (encountered in ULF MRI) to surface-coil design (e.g., the gradient coils in MRI) and field interpolation in the free space (useful for visualizing and modeling neuronal fields).



## 5. Discussion

Both magnetoencephalography and ultra-low-field MRI are somewhat limited in the spatial resolution for imaging magnetic sources. Despite this fact, their combination in a single device can provide unique possibilities for magnetic brain imaging. Understanding the field recorded by a multichannel magnetometer is crucial for developing new methods that can take full advantage of combination of these two modalities.

In MEG, considering the measurement in terms of reciprocal vector fields enables the interpretation of linear source estimates and their spatial resolution. The spatial dependence of the magnetic lead field is mainly determined by the orientation and the location of the sensor with respect to the inner skull of the head. Thus, errors in the co-registration of the MRI-derived head model and the magnetic sensors can play a big role in the spatial accuracy of MEG. In Publication I, the issues with co-registration were alleviated by the spatial calibration of the MEG–MRI device, which removes the need for complicated co-registration stages. Although the minimum-norm estimation may not be so sensitive to spatial errors, the enhanced spatial accuracy is useful when source estimation methods involving additional prior information are applied.

The improved spatial accuracy in MEG using the hybrid MEG–MRI device is based on the assumption that ULF-MR data can be used to construct the head model for MEG. Because of the issues discussed in Sec. 3.4.1, similar resolution to high-field MRI can be difficult to obtain in a reasonable imaging time. However, constructing the over-all shape of the head, especially that of the inner skull, is doable also using lower-resolution data. Because ULF MRI in the hybrid device can provide this information without a need for co-registration, it can still enhance the spatial accuracy of MEG. Additionally, the workflow of the measurement and data processing in MEG can be simplified.

The spatial resolution of bioelectromagnetic neuroimaging could be further increased by combining MEG with EEG [84]. The promise of ULF MRI for this combination is that current-density imaging can provide information for improving the volume conductor model essential especially for

EEG. Theoretically, as the EEG lead fields correspond to the field pattern produced by applying a current between pairs of electrodes, CDI can directly measure these patterns. In practice, as shown in Publication II, the SNR and spatial resolution of CDI may not be high-enough for resolving the currents adequately. Nevertheless, image data of  $\vec{B}_J$  could be used to resolve the flux of current passing the skull, because these patterns are known to be spatially smooth a priori. Furthermore, the (multi-)electrode configuration [85, 86] and the electrodes themselves [87, 88] could be optimized for higher intracranial current and reduced sensation of the current on the skin. Combining the methodological and technical improvements, individual differences due to the structure of the skull could be measured and applied for modeling EEG.

In Publication III, the spatial information of MEG was studied in terms of field patterns sampled on surface around the head. The results of this study suggest that bringing the sensors on the scalp, e.g., by means of, optically-pumped magnetometers, increases the spatial-frequency content of the field by roughly a factor of three. Could ULF MRI benefit from sensors closer to the head, too? First, the sensitivity of the measurements would increase, especially very close to the sensor. The increased amount of spatial information could also be used to accelerate the imaging. However, the sensor types currently applied for MEG would not work as they require a magnetic field stabilized from low-frequency field fluctuations. Although these sensors can be tuned for a desired frequency for the detection of MR signal [89, 90], they need to be shielded from the fields of the MR sequence which complicates the construction of a whole-head device. Another problem in applying these sensors for MRI is their limited bandwidth.

A common aspect in field distributions such as the potential distribution in EEG, the magnetic field distribution in MEG, and the flux of current at the inner skull in CDI is that they are limited to low spatial frequencies. In the usual sense, spatial frequencies are associated with sinusoidal functions in certain coordinate systems, such as Cartesian or spherical ones. In Publication III and Publication IV, spatial-frequency methods were generalized on curved geometries using the Laplace–Beltrami eigenfunctions, which have been used in graphics and geometry processing for some time [91, 92, 31]. These functions can provide useful bases for problems related to smooth surface fields in bioelectromagnetic neuroimaging. Furthermore, the functions could be used to parametrize small disturbances in the geometry itself, which could provide a different approach to determine curved geometries from structural MR data.

## 6. Conclusions

In this Thesis, computational modeling of the magnetic field was applied for developing methods that facilitate the design and analysis of magnetic brain imaging. For ultra-low-field MRI, a sensitivity-field-based spatial calibration method was introduced and the signal-to-noise ratio of current-density imaging of the human head was analyzed. For magnetoencephalography, generalized spatial-frequency analysis and an optimal design were applied to study the spatial sampling of neuronal magnetic fields. Last, computational tools for magnetic-field design and analysis were developed and published also as a software package.



# References

- [1] P. L. Nunez and R. Srinivasan, *Electric Fields of the Brain: the Neurophysics of EEG*. Oxford University Press, USA, 2006.
- [2] M. Hämäläinen, R. Hari, R. J. Ilmoniemi, J. Knuutila, and O. V. Lounasmaa, “Magnetoencephalography—theory, instrumentation, and applications to noninvasive studies of the working human brain,” *Reviews of Modern Physics*, vol. 65, no. 2, pp. 413–497, 1993.
- [3] V. S. Zotev, A. N. Matlashov, P. L. Volegov, I. M. Savukov, M. A. Espy, J. C. Mosher, J. J. Gomez, and R. H. Kraus, “Microtesla MRI of the human brain combined with MEG,” *Journal of Magnetic Resonance*, vol. 194, pp. 115–120, 2008.
- [4] P. T. Vesonen, J. O. Nieminen, K. C. J. Zevenhoven, J. Dabek, L. T. Parkkonen, A. V. Zhdanov, J. Luomahaara, J. Hassel, J. Penttilä, J. Simola, *et al.*, “Hybrid ultra-low-field MRI and magnetoencephalography system based on a commercial whole-head neuromagnetometer,” *Magnetic Resonance in Medicine*, vol. 69, no. 6, pp. 1795–1804, 2013.
- [5] J. Clarke, M. Hatridge, and M. Mölle, “SQUID-detected magnetic resonance imaging in microtesla fields,” *Annual Review of Biomedical Engineering*, vol. 9, pp. 389–413, 2007.
- [6] M. Espy, A. Matlashov, and P. Volegov, “SQUID-detected ultra-low field MRI,” *Journal of Magnetic Resonance*, vol. 229, pp. 127 – 141, 2013.
- [7] H. A. Haus and J. R. Melcher, *Electromagnetic Fields and Energy*. Prentice Hall Englewood Cliffs, NJ, 1989.
- [8] J. D. Jackson, *Classical Electrodynamics*. John Wiley & Sons, 3rd ed., 1999.
- [9] R. Plonsey and D. B. Heppner, “Considerations of quasi-stationarity in electrophysiological systems,” *The Bulletin of Mathematical Biophysics*, vol. 29, no. 4, pp. 657–664, 1967.
- [10] R. J. Ilmoniemi and J. Sarvas, *Brain Signals: Physics and Mathematics of MEG and EEG*. MIT Press, 2019.
- [11] J. Malmivuo and R. Plonsey, *Bioelectromagnetism: Principles and Applications of Bioelectric and Biomagnetic Fields*. Oxford University Press, 1995.
- [12] M. Stenroos and A. Nummenmaa, “Incorporating and compensating cerebrospinal fluid in surface-based forward models of magneto-and electroencephalography,” *PLoS One*, vol. 11, no. 7, p. e0159595, 2016.

- [13] C. H. Wolters, A. Anwander, X. Tricoche, D. Weinstein, M. A. Koch, and R. S. MacLeod, "Influence of tissue conductivity anisotropy on EEG/MEG field and return current computation in a realistic head model: a simulation and visualization study using high-resolution finite element modeling," *Neuroimage*, vol. 30, no. 3, pp. 813–826, 2006.
- [14] J. Kybic, M. Clerc, T. Abboud, O. Faugeras, R. Keriven, and T. Papadopoulos, "A common formalism for the integral formulations of the forward EEG problem," *IEEE Transactions on Medical Imaging*, vol. 24, no. 1, pp. 12–28, 2005.
- [15] M. Stenroos, V. Mäntynen, and J. Nenonen, "A Matlab library for solving quasi-static volume conduction problems using the boundary element method," *Computer Methods and Programs in Biomedicine*, vol. 88, pp. 256–263, Dec. 2007.
- [16] D. B. Geselowitz, "On bioelectric potentials in an inhomogeneous volume conductor," *Biophysical Journal*, vol. 7, no. 1, pp. 1–11, 1967.
- [17] D. Geselowitz, "On the magnetic field generated outside an inhomogeneous volume conductor by internal current sources," *IEEE Transactions on Magnetism*, vol. 6, no. 2, pp. 346–347, 1970.
- [18] T. F. Oostendorp, J. Delbeke, and D. F. Stegeman, "The conductivity of the human skull: results of in vivo and in vitro measurements," *IEEE Transactions on Biomedical Engineering*, vol. 47, no. 11, pp. 1487–1492, 2000.
- [19] M. Akhtari, H. Bryant, A. Mamelak, E. Flynn, L. Heller, J. Shih, M. Mandelkem, A. Matlachov, D. Ranken, E. Best, *et al.*, "Conductivities of three-layer live human skull," *Brain Topography*, vol. 14, no. 3, pp. 151–167, 2002.
- [20] M. S. Hämäläinen and J. Sarvas, "Realistic conductivity geometry model of the human head for interpretation of neuromagnetic data," *IEEE transactions on Biomedical Engineering*, vol. 36, no. 2, pp. 165–171, 1989.
- [21] A. Abragam, *The Principles of Nuclear Magnetism*. Oxford University Press, 1961.
- [22] R. W. Brown, Y.-C. N. Cheng, E. M. Haacke, M. R. Thompson, and R. Venkatesan, *Magnetic resonance imaging: physical principles and sequence design*. John Wiley & Sons, 2014.
- [23] P. Hömmen, J.-H. Storm, N. Höfner, and R. Körber, "Demonstration of full tensor current density imaging using ultra-low field MRI," *Magnetic Resonance Imaging*, vol. 60, pp. 137–144, 2019.
- [24] J. Bronzan, "The magnetic scalar potential," *American Journal of Physics*, vol. 39, no. 11, pp. 1357–1359, 1971.
- [25] O. D. Kellogg, *Foundations of Potential Theory*. Courier Corporation, 1953.
- [26] R. J. Blakely, *Potential Theory in Gravity and Magnetic applications*. Cambridge University Press, 1996.
- [27] S. Taulu and M. Kajola, "Presentation of electromagnetic multichannel data: the signal space separation method," *Journal of Applied Physics*, vol. 97, no. 12, p. 124905, 2005.
- [28] R. Zetter, A. J. Mäkinen, J. Iivanainen, K. C. J. Zevenhoven, R. J. Ilmoniemi, and L. Parkkonen, "Magnetic field modeling with surface currents. Part II. Implementation and usage of bfieldtools," *Journal of Applied Physics*, vol. 128, no. 6, p. 063905, 2020.

- [29] W. Hackbusch, *Integral Equations: Theory and Numerical Treatment*. Birkhäuser, Berlin, 1995.
- [30] G. Peeren, *Stream function approach for determining optimal surface currents*. PhD thesis, Philips Research, 2003.
- [31] B. Vallet and B. Lévy, “Spectral geometry processing with manifold harmonics,” in *Computer Graphics Forum*, vol. 27, pp. 251–260, Wiley Online Library, 2008.
- [32] W. Myers, D. Slichter, M. Hatridge, S. Busch, M. Mößle, R. McDermott, A. Trabesinger, and J. Clarke, “Calculated signal-to-noise ratio of MRI detected with SQUIDS and Faraday detectors in fields from 10  $\mu$ T to 1.5 T,” *Journal of Magnetic Resonance*, vol. 186, no. 2, pp. 182–192, 2007.
- [33] J. Clarke and A. I. Braginski, *The SQUID handbook. Vol. 1, Fundamentals and Technology of SQUIDS and SQUID Systems*. Wiley-VCH, 2004.
- [34] T. M. Tierney, N. Holmes, S. Mellor, J. D. López, G. Roberts, R. M. Hill, E. Boto, J. Leggett, V. Shah, M. J. Brookes, R. Bowtell, and G. R. Barnes, “Optically pumped magnetometers: From quantum origins to multi-channel magnetoencephalography,” *Neuroimage*, vol. 199, pp. 598 – 608, 2019.
- [35] M. Pannetier, C. Fermon, G. Le Goff, J. Simola, and E. Kerr, “Femtotesla magnetic field measurement with magnetoresistive sensors,” *Science*, vol. 304, no. 5677, pp. 1648–1650, 2004.
- [36] F. Öisjöen, J. F. Schneiderman, G. Figueras, M. Chukharkin, A. Kalabukhov, A. Hedström, M. Elam, and D. Winkler, “High- $T_c$  superconducting quantum interference device recordings of spontaneous brain activity: Towards high- $T_c$  magnetoencephalography,” *Applied Physics Letters*, vol. 100, no. 13, p. 132601, 2012.
- [37] K. C. J. Zevenhoven, A. J. Mäkinen, and R. J. Ilmoniemi, “Superconducting receiver arrays for magnetic resonance imaging,” *Biomedical Physics & Engineering Express*, vol. 6, no. 1, p. 015016, 2020.
- [38] G. Nolte, “The magnetic lead field theorem in the quasi-static approximation and its use for magnetoencephalography forward calculation in realistic volume conductors,” *Physics in Medicine and Biology*, vol. 48, no. 22, pp. 3637–3652, 2003.
- [39] S. Vallaghé, T. Papadopoulou, and M. Clerc, “The adjoint method for general EEG and MEG sensor-based lead field equations,” *Physics in Medicine & Biology*, vol. 54, no. 1, p. 135, 2008.
- [40] A. J. Woods, A. Antal, M. Bikson, P. S. Boggio, A. R. Brunoni, P. Celnik, L. G. Cohen, F. Fregni, C. S. Herrmann, E. S. Kappenman, *et al.*, “A technical guide to tDCS, and related non-invasive brain stimulation tools,” *Clinical neurophysiology*, vol. 127, no. 2, pp. 1031–1048, 2016.
- [41] L. Heller and D. B. van Hulsteyn, “Brain stimulation using electromagnetic sources: theoretical aspects,” *Biophysical Journal*, vol. 63, no. 1, pp. 129–138, 1992.
- [42] K. P. Pruessmann, “Encoding and reconstruction in parallel MRI,” *NMR in Biomedicine*, vol. 19, pp. 288–299, May 2006.
- [43] G. Backus and F. Gilbert, “The resolving power of gross earth data,” *Geophysical Journal International*, vol. 16, no. 2, pp. 169–205, 1968.

- [44] B. Lütkenhöner and R. G. de Peralta Menendez, “The resolution-field concept,” *Electroencephalography and clinical Neurophysiology*, vol. 102, no. 4, pp. 326–334, 1997.
- [45] O. Hauk and M. Stenroos, “A framework for the design of flexible cross-talk functions for spatial filtering of EEG/MEG data: DeFleCT,” *Human Brain Mapping*, vol. 35, no. 4, pp. 1642–1653, 2014.
- [46] K. P. Pruessmann, M. Weiger, M. B. Scheidegger, and P. Boesiger, “SENSE: Sensitivity encoding for fast MRI,” *Magnetic Resonance in Medicine*, vol. 42, no. 5, pp. 952–962, 1999.
- [47] F.-H. Lin, P. T. Vesänen, J. O. Nieminen, Y.-C. Hsu, K. C. J. Zevenhoven, J. Dabek, L. T. Parkkonen, A. Zhdanov, and R. J. Ilmoniemi, “Noise amplification in parallel whole-head ultra-low-field magnetic resonance imaging using 306 detectors,” *Magnetic Resonance in Medicine*, vol. 70, no. 2, pp. 595–600, 2013.
- [48] B. Lütkenhöner, “Magnetoencephalography and its Achilles’ heel,” *Journal of Physiology-Paris*, vol. 97, pp. 641–658, July 2003.
- [49] F.-H. Lin, J. W. Belliveau, A. M. Dale, and M. S. Hämäläinen, “Distributed current estimates using cortical orientation constraints,” *Human Brain Mapping*, vol. 27, no. 1, pp. 1–13, 2006.
- [50] F.-H. Lin, T. Witzel, S. P. Ahlfors, S. M. Stufflebeam, J. W. Belliveau, and M. S. Hämäläinen, “Assessing and improving the spatial accuracy in MEG source localization by depth-weighted minimum-norm estimates,” *Neuroimage*, vol. 31, no. 1, pp. 160–171, 2006.
- [51] S. Sommariva and A. Sorrentino, “Sequential Monte Carlo samplers for semi-linear inverse problems and application to magnetoencephalography,” *Inverse Problems*, vol. 30, no. 11, p. 114020, 2014.
- [52] B. D. Van Veen, W. Van Drongelen, M. Yuchtman, and A. Suzuki, “Localization of brain electrical activity via linearly constrained minimum variance spatial filtering,” *IEEE Transactions on Biomedical Engineering*, vol. 44, no. 9, pp. 867–880, 1997.
- [53] A. Hillebrand and G. R. Barnes, “The use of anatomical constraints with MEG beamformers,” *Neuroimage*, vol. 20, no. 4, pp. 2302–2313, 2003.
- [54] A. Hillebrand and G. R. Barnes, “Practical constraints on estimation of source extent with MEG beamformers,” *Neuroimage*, vol. 54, no. 4, pp. 2732–2740, 2011.
- [55] F. Chella, L. Marzetti, M. Stenroos, L. Parkkonen, R. J. Ilmoniemi, G. L. Romani, and V. Pizzella, “The impact of improved MEG–MRI co-registration on MEG connectivity analysis,” *Neuroimage*, vol. 197, pp. 354–367, 2019.
- [56] B. Vanrumste, G. Van Hoey, R. Van de Walle, M. D’havé, I. Lemahieu, and P. Boon, “Dipole location errors in electroencephalogram source analysis due to volume conductor model errors,” *Medical and Biological Engineering and Computing*, vol. 38, no. 5, pp. 528–534, 2000.
- [57] F. Chen, H. Hallez, and S. Staelens, “Influence of skull conductivity perturbations on EEG dipole source analysis,” *Medical Physics*, vol. 37, no. 8, pp. 4475–4484, 2010.
- [58] M. Stenroos, A. Hunold, and J. Haueisen, “Comparison of three-shell and simplified volume conductor models in magnetoencephalography,” *NeuroImage*, vol. 94, pp. 337–348, 2014.

- [59] A. I. Ahonen, M. S. Hämäläinen, R. J. Ilmoniemi, M. Kajola, J. E. T. Knuutila, J. Simola, and V. V. A., “Sampling theory for neuromagnetic detector arrays,” *IEEE Transactions on Biomedical Engineering*, vol. 40, no. 9, pp. 859–869, 1993.
- [60] D. V. Lindley, “On a measure of the information provided by an experiment,” *The Annals of Mathematical Statistics*, vol. 27, no. 4, pp. 986–1005, 1956.
- [61] P. Kemppainen and R. Ilmoniemi, “Channel capacity of multichannel magnetometers,” in *Advances in Biomagnetism*, pp. 635–638, Springer, 1989.
- [62] J. O. Nieminen, P. T. Vesanen, K. C. J. Zevenhoven, J. Dabek, J. Hassel, J. Luomahaara, J. S. Penttilä, and R. J. Ilmoniemi, “Avoiding eddy-current problems in ultra-low-field MRI with self-shielded polarizing coils,” *Journal of Magnetic Resonance*, vol. 212, no. 1, pp. 154–160, 2011.
- [63] K. C. J. Zevenhoven, H. Dong, R. J. Ilmoniemi, and J. Clarke, “Dynamical cancellation of pulse-induced transients in a metallic shielded room for ultra-low-field magnetic resonance imaging,” *Applied Physics Letters*, vol. 106, no. 3, pp. 034101–034101, 2015.
- [64] J. Luomahaara, P. T. Vesanen, J. Penttilä, J. O. Nieminen, J. Dabek, J. Simola, M. Kiviranta, L. Grönberg, K. C. J. Zevenhoven, R. J. Ilmoniemi, and J. Hassel, “All-planar SQUIDS and pickup coils for combined MEG and MRI,” *Superconductor Science and Technology*, vol. 24, no. 7, pp. 075020–075020, 2011.
- [65] J. Luomahaara, M. Kiviranta, L. Grönberg, K. C. J. Zevenhoven, and P. Laine, “Unshielded SQUID sensors for ultra-low-field magnetic resonance imaging,” *IEEE Transactions on Applied Superconductivity*, vol. 28, no. 4, pp. 1–4, 2018.
- [66] S. K. Lee, M. Mölle, W. Myers, N. Kelso, A. H. Trabesinger, A. Pines, and J. Clarke, “SQUID-detected MRI at 132  $\mu$ T with T1-weighted contrast established at 10  $\mu$ T–300 mT,” *Magnetic Resonance in Medicine*, vol. 53, no. 1, pp. 9–14, 2005.
- [67] V. S. Zotev, A. N. Matlashov, I. M. Savukov, T. Owens, P. L. Volegov, J. J. Gomez, and M. A. Espy, “SQUID-based microtesla MRI for in vivo relaxometry of the human brain,” *IEEE Transactions on Applied Superconductivity*, vol. 19, no. 3, pp. 823–826, 2009.
- [68] S. Busch, M. Hatridge, M. Mölle, W. Myers, T. Wong, M. Mück, K. Chew, K. Kuchinsky, J. Simko, and J. Clarke, “Measurements of T1-relaxation in ex vivo prostate tissue at 132  $\mu$ T,” *Magnetic Resonance in Medicine*, vol. 67, no. 4, pp. 1138–1145, 2012.
- [69] K. C. J. Zevenhoven and S. Alanko, “Ultra-low-noise amplifier for ultra-low-field MRI main field and gradients,” in *Journal of Physics: Conference Series*, vol. 507, pp. 042050–042050, 2014.
- [70] M. Espy, A. Matlashov, and P. Volegov, “SQUID-detected ultra-low field MRI,” *Journal of Magnetic Resonance*, vol. 229, pp. 127–141, 2013.
- [71] P. L. Volegov, J. C. Mosher, M. A. Espy, and R. H. Kraus, “On concomitant gradients in low-field MRI,” *Journal of Magnetic Resonance*, vol. 175, no. 1, pp. 103–113, 2005.
- [72] R. Kraus Jr, M. Espy, P. Magnelind, and P. Volegov, *Ultra-Low Field Nuclear Magnetic Resonance: A New MRI Regime*. Oxford University Press, 2014.

- [73] Y. C. Hsu, P. T. Vesanen, J. O. Nieminen, K. C. J. Zevenhoven, J. Dabek, L. Parkkonen, I. L. Chern, R. J. Ilmoniemi, and F. H. Lin, "Efficient concomitant and remanence field artifact reduction in ultra-low-field MRI using a frequency-space formulation," *Magnetic Resonance in Medicine*, vol. 71, no. 3, pp. 955–965, 2014.
- [74] R. Körber, J. O. Nieminen, N. Höfner, V. Jazbinšek, H.-J. Scheer, K. Kim, and M. Burghoff, "An advanced phantom study assessing the feasibility of neuronal current imaging by ultra-low-field NMR," *Journal of Magnetic Resonance*, vol. 237, pp. 182–190, 2013.
- [75] L. Heller, B. E. Barrowes, and J. S. George, "Modeling direct effects of neural current on MRI," *Human Brain Mapping*, vol. 30, no. 1, pp. 1–12, 2009.
- [76] G. Vranou, "Assessing the value of a priori information in solving the MEG inverse problem," Master's thesis, Aalto University School of Science, 2019.
- [77] M. Joy, G. Scott, and M. Henkelman, "In vivo detection of applied electric currents by magnetic resonance imaging," *Magnetic Resonance Imaging*, vol. 7, no. 1, pp. 89 – 94, 1989.
- [78] P. T. Vesanen, J. O. Nieminen, K. C. J. Zevenhoven, Y.-C. Hsu, and R. J. Ilmoniemi, "Current-density imaging using ultra-low-field MRI with zero-field encoding," *Magnetic Resonance Imaging*, vol. 32, no. 6, pp. 766–770, 2014.
- [79] M. Bikson, P. Grossman, C. Thomas, A. L. Zannou, J. Jiang, T. Adnan, A. P. Mourdoukoutas, G. Kronberg, D. Truong, P. Boggio, A. R. Brunoni, L. Charvet, F. Fregni, B. Fritsch, B. Gillick, R. H. Hamilton, B. M. Hampstead, R. Jankord, A. Kirton, H. Knotkova, D. Liebetanz, A. Liu, C. Loo, M. A. Nitsche, J. Reis, J. D. Richardson, A. Rotenberg, P. E. Turkeltaub, and A. J. Woods, "Safety of transcranial direct current stimulation: Evidence based update 2016," *Brain Stimulation*, vol. 9, no. 5, pp. 641 – 661, 2016.
- [80] P. C. Miranda, M. Lomarev, and M. Hallett, "Modeling the current distribution during transcranial direct current stimulation," *Clinical Neurophysiology*, vol. 117, no. 7, pp. 1623–1629, 2006.
- [81] C. Whalen, E. L. Maclin, M. Fabiani, and G. Gratton, "Validation of a method for coregistering scalp recording locations with 3D structural MR images," *Human Brain Mapping*, vol. 29, no. 11, pp. 1288–1301, 2008.
- [82] H. Sonntag, J. Haueisen, and B. Maess, "Quality assessment of MEG-to-MRI coregistrations," *Physics in Medicine & Biology*, vol. 63, no. 7, p. 075003, 2018.
- [83] R. Guidotti, R. Sinibaldi, C. De Luca, A. Conti, R. J. Ilmoniemi, K. C. J. Zevenhoven, P. E. Magnelind, V. Pizzella, C. Del Gratta, G. L. Romani, and S. Della Penna, "Optimized 3D co-registration of ultra-low-field and high-field magnetic resonance images," *PloS One*, vol. 13, no. 3, 2018.
- [84] A. Molins, S. M. Stufflebeam, E. N. Brown, and M. S. Hämläinen, "Quantification of the benefit from integrating MEG and EEG data in minimum l2-norm estimation," *Neuroimage*, vol. 42, no. 3, pp. 1069–1077, 2008.
- [85] J. P. Dmochowski, A. Datta, M. Bikson, Y. Su, and L. C. Parra, "Optimized multi-electrode stimulation increases focality and intensity at target," *Journal of Neural Engineering*, vol. 8, no. 4, p. 046011, 2011.
- [86] A. Hunold, D. Ortega, K. Schellhorn, and J. Haueisen, "Novel flexible cap for application of transcranial electrical stimulation: a usability study," *Biomedical Engineering Online*, vol. 19, no. 50, 2020.

- [87] G. Kronberg and M. Bikson, "Electrode assembly design for transcranial direct current stimulation: a FEM modeling study," in *2012 Annual International Conference of the IEEE Engineering in Medicine and Biology Society*, pp. 891–895, IEEE, 2012.
- [88] V. T. Krasteva and S. P. Papazov, "Estimation of current density distribution under electrodes for external defibrillation," *Biomedical Engineering Online*, vol. 1, no. 1, pp. 1–13, 2002.
- [89] I. Savukov, V. Zotev, P. Volegov, M. Espy, A. Matlashov, J. Gomez, and R. Kraus Jr, "MRI with an atomic magnetometer suitable for practical imaging applications," *Journal of Magnetic Resonance*, vol. 199, no. 2, pp. 188–191, 2009.
- [90] I. M. Savukov, S. Seltzer, M. V. Romalis, and K. Sauer, "Tunable atomic magnetometer for detection of radio-frequency magnetic fields," *Physical review letters*, vol. 95, no. 6, p. 063004, 2005.
- [91] B. Levy, "Laplace-Beltrami eigenfunctions towards an algorithm that "understands" geometry," in *IEEE International Conference on Shape Modeling and Applications 2006 (SMI'06)*, pp. 13–13, IEEE, 2006.
- [92] M. Reuter, S. Biasotti, D. Giorgi, G. Patanè, and M. Spagnuolo, "Discrete Laplace–Beltrami operators for shape analysis and segmentation," *Computers & Graphics*, vol. 33, no. 3, pp. 381–390, 2009.





ISBN 978-952-64-0109-6 (printed)

ISBN 978-952-64-0110-2 (pdf)

ISSN 1799-4934 (printed)

ISSN 1799-4942 (pdf)

**Aalto University**

**School of Science**

**Department of Neuroscience and Biomedical Engineering**

[www.aalto.fi](http://www.aalto.fi)

**BUSINESS +  
ECONOMY**

**ART +  
DESIGN +  
ARCHITECTURE**

**SCIENCE +  
TECHNOLOGY**

**CROSSOVER**

**DOCTORAL  
DISSERTATIONS**